DELFT UNIVERSITY OF TECHNOLOGY

MSE THESIS
MS53035

Thesis

Mechanical stability of Pd/Ti thin films during hydrogen (de)sorption at different applied partial pressure levels of hydrogen

Student name: Chi Chang
Student ID: 5133483

Supervisor: Dr. Amarante Böttger (TU Delft, Department of Material Science & Engineering)

Thesis committee:
Dr. Amarante Böttger (TU Delft, Department of Material Science & Engineering)
Prof. Dr. Ir. J. Sietsma (TU Delft, Department of Material Science & Engineering)

August 25, 2021

TU Delft Delft University of Technology

Contents

Acronyms

BCDI Bragg coherent diffractive imaging

FWHM The width of the line profile at half the maximum intensity

HRTEM High Resolution TEM

M-H Metal-Hydrogen system

mod-WH modified Williamson-Hall

Pd-H Palladium-Hydrogen ststem

PCT Pressure, Composition & Temperature Isotherm

XRD X-Ray Diffractometry

1. Abstract

In this work, mechanical stability and kinetics of hydrogen (de)sorption of thin Palladium films (∼100 nm) magnetron sputter deposited on a magnetron sputtered Titanium intermediate layer were studied. In particular of two film morphologies, an open voided columnar morphology and a compact columnar morphology, the substrate-induced stress and its relaxation upon hydride formation were investigated at room temperature.

By conducting in-situ X-ray diffraction (XRD) measurements combined with line-broadening analysis of the diffraction profiles, it was observed that the α (H-poor phase) to β (H-rich phase) transition induces stress that could (partially) relax by dislocation generation. After several absorption-desorption cycles (at 0.05 atm $p(H_2)$), however, this stress increase prevents a full transformation to the β phase. When applying a higher partial pressure $p(H_2) = 0.1$ atm for both of the selected open and compact-structured Pd/Ti thin films, a full phase transformation was observed. The corresponding phase transition kinetics, stress states and microstructural behaviors of the open and compact-structured Pd/Ti samples were found to be different. The microstructural changes and the kinetics of phase transformation during H_2 (de)sorption are explained in terms of stress development and its relaxation through dislocation/defect generation.

2. Introduction

Recently, Palladium (Pd) has been reported to play a major role in the point of view of hydrogen economy owing to its intrinsic catalytic and hydrogen absorbing characteristics [1] [2]. In addition, both of the catalytic and hydrogen absorbing properties could be sustained at low pressure and room temperature [1] [2] [3]. Thus, Pd and its alloys become a suitable candidate for the applications of hydrogen sensors [4] [5], hydrogen storage [6] [7], hydrogen purification [8] and fuel cell catalysts [9]. However, Pd is not extensively applied in the industry of above-mentioned fields since several important requirements are currently not satisfied, such as operability at different conditions (temperature and pressure) [10] [11], cost-efficiency [1] [11] [12] and the issue of hydrogen embrittlement [12].

Many studies have shown that microstructure dictates the H_2 absorption and desorption properties for several metal-hydrogen (M-H) system including the Pd-H system [13]. In this research, Pundt and Kirchheim stated that different types of hydrogen trapping sites are provided by various microstructures such as bulk or nanostructured thin films. Furthermore, nanostructured Pd is proven to have a high hydrogen diffusivity owing to grain boundaries which act as fast diffusion pathways [14] [15]. On the other hand, other researches revealed that crystallographic defects (such as dislocations) strongly affect the properties of nanosized Pd [16] [17] [18]. In the meantime, durability of nanostructured Pd under large stress induced by the large volume changes during H_2 absorption and desorption is sustained due to the ability of removing crystallographic imperfections for Pd nanoparticles [16] [17]. It was also reported that these imperfections act as an extra energy barrier for the phase transitions for both Pd nanoparticles [17] and Pd nanocrystalline films [19].

In the previous work regarding Pd thin films, Verma et al. demonstrated that morphology of the films (open versus compact columnar structure) and clamping effect significantly affect the mechanical stability of the films during H_2 loading and deloading cycles at room temperature [18]. The occurrence of clamping effect is owing to both the large mechanical stress induced by the large volume expansion while absorbing H_2 and the substrate-induced elastic constrain [20] [21]. Without clamping effect (constrain) induced by substrates, it was found that buckling or film detachment occurred in compact-structured Pd films due to large internal stress during H_2 absorption and desorption [18]. However, for open-structured Pd films, the films remain flat since the stress can be accommodated by the voids along the grain boundaries [18].

In the same research work done by Verma et al., Pd thin films with titanium (Ti) as a strongly adhesive intermediate layer were also studied. It was shown that both morphology and clamping effect also dramatically influenced H_2 absorbing properties of the films. For the compact structured Pd on Ti, it was discovered that the kinetics of the α (hydrogen-poor phase) - β (hydrogen-rich phase) phase transition is very slow and incomplete (α phase was not fully transformed under H_2 loading condition with partial pressure of hydrogen of 0.05 atm) [22]. The slow hydriding process is attributed to both of the above-mentioned contributors which restrict lateral film expansion to form β phase and induce high compressive stress. By contrast, the α - β phase transition is found to be completed in 20 minutes for Pd with open structure on Ti layer. In this case, the void-rich structured Pd/Ti films provide free space for the expansion and release of stress. Hence, the substrate-induced clamping effect is surpassed by the open morphology, and the hydriding process can be accelerated, consequently.

As mentioned in the previous two paragraphs, the impacts of morphology and clamping effect on the mechanical stability and H_2 absorbing properties were studied. Furthermore, research of the thermal stability of the Pd films on Ti was also conducted in the same report. However, the influence of different partial pressures of hydrogen ($p(H_2)$) on Pd/Ti thin films during H_2 absorption and desorption has not been researched yet. According to the pressure, composition, and temperature (PCT) isotherm of Pd-H system shown in Figure 2.1, the α - β phase transition should be completed at room temperature (20 °C) when $p(H_2)$ is higher than the plateau pressure (roughy 0.006 atm). Nevertheless, in the work done by Verma et al., it was shown that the α - β phase transition could not be completed for the Pd/Ti thin films with a compact structure at room temperature while $p(H_2)$ of 0.05 atm was applied which is approximately one order of magnitude higher than the plateau pressure. From the result, it is clear that the energy barrier of the α - β phase transition during H_2 absorption for the compact Pd/Ti thin films is remarkably higher than pure palladium-hydrogen system. The underlying cause of the phenomenon will be discussed in 3.1.

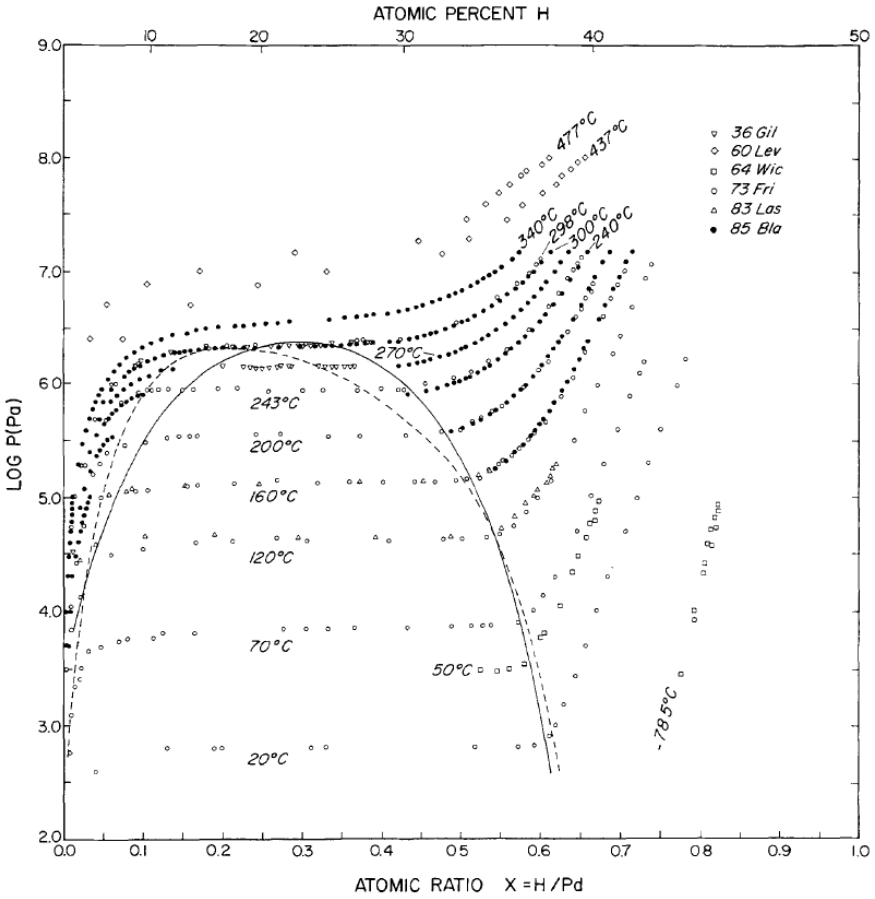

Figure 2.1: A PCT diagram of the Pd-H system. The left side of the diagram is corresponding to the α phase (low H concentration), and the right side of it represents the β phase (high H concentration). The dashed and solid curves are the different fits from different authors. The data points of all the isotherms in the coexistence region are measured during desorption of hydrogen. Ref: [3]

In view of the current literature, the differences of microstructural behaviors for open and compact-structured Pd/Ti thin films during H_2 loading and deloading cycles, applying different $p(H_2)$, are going to be investigated. In order to observe the kinetics of the α - β phase transition, the stress states and dislocation-mediated deformation of the Pd/Ti thin films during hydrogen absorption and desorption, in-situ hydriding experiments using X-ray diffractometry (XRD) are conducted. This will be further explained in section 4.

3. Theoretical background and research questions

3.1. Theoretical background

According to a study based on positron annihilation spectroscopy combined with electron microscopy and XRD, it was discovered that stress relaxation occurs during hydrogenation of Pd films [23]. Furthermore, since buckling was not observed for Pd/Ti thin films while absorbing H_2 [18], dislocation emissions are found to play a dominant role in releasing the large built-up internal compressive stress induced by both clamping effect, and lattice expansion of the α-β phase transition [18] [21]. As a result, the energy barrier of the α-β phase transition in the Pd-H system is strongly affected [21]. It could be assumed that this energy barrier could be overcome by a specific applied p(H_2) since the chemical potential of hydrogen in the gas phase (μ_{HH}) could be assumed to be equal to the chemical potential of hydrogen in the metal (μ_H) [24]. The relationship between μ_{HH} and μ_H is given in Equation 3.1 [24]:

$$\mu_{HH} = \frac{1}{2}[\mu^0_{HH} + RT \ln \frac{p_{HH}}{p^0_{HH}}] = \mu_H \tag{3.1}$$

where R is the gas constant of hydrogen, T is the absolute temperature, p_{HH} is the pressure of hydrogen gas (assumed to be an ideal gas), and the superscript of 0 represents the standard state.

According to Wagner and Pundt [21], a linear approximation of the chemical potential μ_H illustrating the energy barrier of the phase transition is given as Equation 3.2:

$$\mu_H = RT \ln \frac{\chi_H}{r - \chi_H} + E_0 - E_{HH}\chi_H - V_0 a_H \sigma_{ii}(\chi_H) \tag{3.2}$$

where χ_H is the hydrogen concentration ([H]/[Pd]) in the Pd-H system. Since palladium exists in a face-centred cubic (fcc) structure, H atoms tend to be dissolved in the interstitial sites with octahedral symmetry [21]. The first term in Equation 3.2 represents the configurational entropy of H dissolved on octahedral interstitial sites in the Pd-H thin films, where r represents the maximum number of sites which could be occupied by H atoms (determined by electronic structure [25] or microstructure [14]). E_0 represents the site energy (more negatively contributed by defects than interstitial sites since the hydrogen atoms tend to be "trapped" at defects) which was assumed to be a constant [21]. E_{HH} is an H-H interaction strength parameter acting against the entropy contribution (represented by the negative sign in the equation) in terms of the contribution to the chemical potential μ_H since H atoms tend to attractively interact through the strain fields of the Pd lattice [26]. The last term in Equation 3.2 illustrates the change of the chemical potential μ_H induced by substrate-induced stress, where V_0 is the partial molar volume of the octahedral sites in Pd occupied by an interstitial H atom, a_H is the lattice expansion factor of Pd induced by H_2 absorption (fixed to be a constant for both V_0 and a_H), and $\sigma_{ii}(\chi_H)$ is the sum of axial stresses as a function of χ_H (assumed to be a mean value obtained for the whole film) [21].

The schematic drawings of the substrate-induced stress and corresponding chemical potential during H_2 absorption including the α-β phase transition is provided in Figure 3.1. As illustrated in Figure 3.1, while the stress increases linearly without stress relaxation as χ_H increases during H_2 absorption ($\sigma_{ii}(\chi_H) = k.\chi_H$, k is a negative constant to represent the Pd thin film was compressively stressed), there is simply an upward shift of the α-β phase transition plateau to a higher chemical potential (represented by μ^*_H in the figure). On the other hand, while stress relaxation occurs, $\sigma_{ii}(\chi_H)$ no longer increases linearly (depicted by the red line in Figure 3.1.a). Hence, the α-β phase transition can start at a lower chemical potential μ_H compared with μ^*_H a sloped plateau (red line in Figure 3.1.b). The local stress relaxation induced by plasticity (dislocation emissions) leads to a step wise reduction of μ_H determined by the local stress state (σ_{ii}) as a function of χ_H (see Equation 3.2). However, according to the figure, μ_H of the substrate-clamped Pd thin film with stress relaxation is still significantly higher than μ_H of bulk Pd. Thus, the chemical potential (corresponding p(H_2) to overcome the chemical potential μ_H [24]) of the α-β phase transition for the compact-structured Pd/Ti thin films (mentioned in section 2) should be much higher than 0.006 atm (see Figure 2.1). Subsequently, the α-β phase transition of the films got "locked in" at the "quasi-equilibrium point" [21] leading to an incomplete α-β phase transition when p(H_2) is 0.05 atm since only the part of the sloped energy barrier (μ_H) lower than the applied p(H_2) could be overcome.

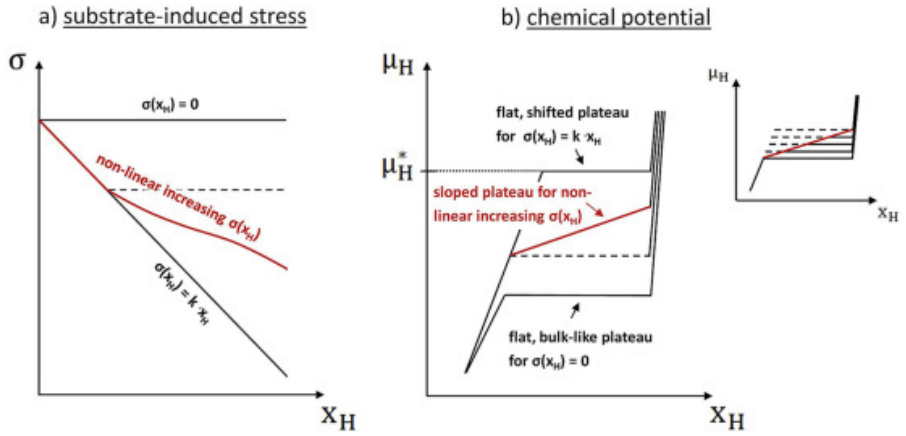

Figure 3.1: The drawings to demonstrate the substrate induced-stress (a) and the chemical potential of the Pd-H system (b) with and without stress relaxation illustrated by the red and black lines, respectively. Ref: [21]

Despite that the emission of dislocations (plasticity) has been concluded to be the main contributor of stress relaxation for Pd/Ti thin film during H_2 absorption [18], the mechanism behind the occurrence of the plasticity remains uncertain. Conducting aberration corrected high resolution TEM (HRTEM) to investigate 150 nm thick nanocrystalline Pd films after hydriding, Amin-Ahmadi et al. [19] stated that the local plasticity was mainly controlled by the dislocation activities when the Pd films were fully hydrided to β phase at $p(H_2) = 0.96$ atm. In the same report, it was also discovered that there was no significant microstructural changes while the Pd films were only hydrided to α phase at $p(H_2) = 0.002$ atm. Nonetheless, another research done by A. Ulvestad and A. Yau [17] using Bragg coherent diffractive imaging (BCDI) to track the nucleation and motion of dislocations for 400 nm synthesized Pd nanoparticles during the α-β phase transition reveals that dislocations are induced in the α phase owing to the large lattice mismatch (approximately 3.5 %) between the α and β phases (both fcc). To further understand at which phase (α or β) the local plasticity induced by dislocations occurs, line broadening analysis of the XRD profile is used to identify the microstructural evolution during the α-β phase transition of the Pd/Ti thin films. The method will be further explained in 4.2.

3.2. Research questions

With the purpose of further understanding the impact of morphology, clamping effect and defects (mainly dislocations emission) on H_2 (de)sorption for different applied $p(H_2)$, the following research questions will be discussed in the following sections:

- With higher $p(H_2)$ applied, could the energy barrier (the sloped plateau depicted in Figure 3.1) of the α-β phase transition be fully overcome during the hydriding process of the Pd/Ti thin films?
- What would be the corresponding stress states and defect (dislocation) densities for the "quasi-equilibrium" phase at H_2 loading/deloading condition when the α-β phase transition is completed and in the case that it is not completed?
- What would be the influence of morphology of the Pd/Ti thin film on the microstructural behavior, and H_2 absorbing/desorbing properties?
- Which phase (α or β) is the main contributor for the source of plasticity (dislocation emission) during H_2 absorption on the Pd/Ti samples?

Further explanations of the methodologies to answer the research questions will be discussed in section 4. Afterwards, the interpretation of the results of kinetic analysis, stress states and microstructural developments during the measured H_2 loading/deloading cycles for the Pd/Ti film samples will also be given. Next, the conclusions for this research and recommendations for future work will be described.

4. Experimental Methodology

4.1. Pd/Ti thin film sample preparation and selection

In this research, two different columnar-structured Pd/Ti thin films characterized by Verma et al. [18] were selected to be analyzed. The preparation of the two Pd thin films is the same as the work done by Verma et al [18] which Pd was deposited by dc magnetron sputtering in an ATC 1500F sputter deposition system from AJA International. For the compact-structured Pd/Ti thin films, Pd was deposited for 480 s at low Ar pressure of 0.4 Pa, and the avaerage deposition rate is 0.2 nm/s. The low deposition pressure was reported to be able to induce high mobility of surface Pd atoms to merge the formed islands and create a continuous compact thin film without voids (see the left figure of Figure 4.1) [18] [27]. On the other hand, Pd was deposited for 900 s at high Ar pressure of 3 Pa with an average deposition rate of 0.1 nm/s for the open-structured Pd/Ti thin film since high deposition rate could decrease the surface mobility of the Pd atoms to generate voided-boundaries separating the columnar structure of Pd thin film as illustrated in the right figure of Figure 4.1 [18] [28]. The base pressure in the deposition chamber was reported to be 1.3×10^{-5} Pa. Thermally oxidized ($\approx$ 188 nm) 2-inch single-crystal Si{100} wafers (Si/SiO_2) were used as a substrate for both of the films. The intermediate adhesive Ti layer was sputter-deposited ($\approx$ 6 nm) between the Si/SiO_2 substrate and the Pd layer at low Ar pressure of 0.4 Pa (compact-structured Pd/Ti) and high Ar pressure of 3 Pa (open-structured Pd/Ti) for 70 s and 360 s, separately. According to the report, all depositions were performed with a substrate temperature close to room temperature ($\approx 20\,^{\circ}\mathrm{C}$).

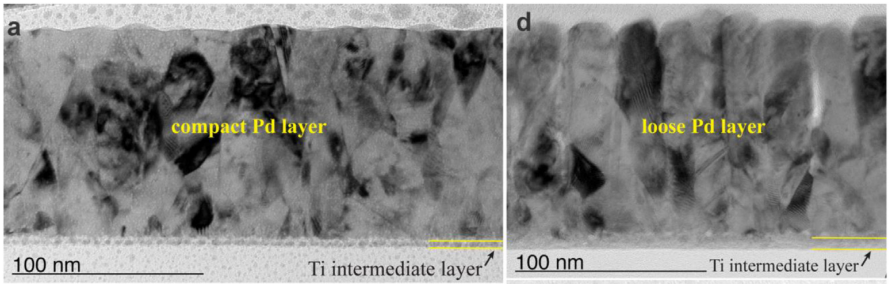

Figure 4.1: A cross-sectional view of TEM bright-field (BF) images (100 nm scale) showing both of the compact-structured Pd/Ti thin film without voids (left figure) and the open-structured Pd/Ti thin film with (nano) voids along the grain boundaries (right figure). Ref: [18]

Regarding the history of the selected Pd/Ti thin film with compact structures, only 1 H_2 loading and deloading cycle was performed previously (start from 2_{nd} loading cycle as shown in Table 4.2). In this case, no significant microstructural evolution is expected before the measurements of this work were started, which means that the occurrence of the incomplete α-β phase transition is still expected to happen with applied p(H_2) = 0.05 atm. For the fresh open-structured Pd/Ti thin films without any previous H_2 absorbing and desorbing cycles, the α-β phase transition was reported to be completed in 20 minutes when p(H_2) is 0.05 atm as discussed in section 2. In this case, it is expected that no significant changes of microstructure will happen by applying higher p(H_2) during H_2 absorption. Therefore, instead of using a fresh Pd/Ti thin film with open structures, the one experienced 20 H_2 loading and deloading cycles (start from 21_{st} loading cycle as illustrated in Table 4.2) was used. This sample has a higher compressive stress and is expected to have a higher energy barrier for the α-β phase transition (as explained in 3.1. The stress results will be provided in 5.1) was selected. The history of the stress states and dislocation density of the selected open-structured Pd/Ti film will be further discussed in section 5.

4.2. X-Ray diffraction (XRD)

Within the scope of this research, in-situ XRD measurements were applied to analyze the changes of stress state, microstructure and kinetics of α-β phase transition of the Pd/Ti thin films during H_2 loading and deloading. Following the framework of the research done by Verma et al. [18], the experiments were conducted on a Bruker-AXS D8 Discover diffractometer equipped with polycapillary optics (0.25°) and Eulerian cradle in parallel beam geometry (CoKα; 45 kV, 25 mA). The data was collected in the ranges of 2θ covering the wanted diffraction

peaks at different sample orientations by tilting the sample at different angles (illustrated by ψ in Figure 4.2 and 4.3). To conduct the analysis effectively within a limited amount of time, a number of different ψ angles were selected separately for short (with only {111}, {200} and {311} peak reflections) and long scans (covering all the diffraction peaks) for all the Pd/Ti film samples as illustrated in Table 4.1. The usage of the data from the scans will be explained in the following sections.

Scan type	**ψ angles**	**Peak reflection**
Short scan	0°, 18.43°, 26.57°, 33.21°, 39.23° and 45°	{111}, {200} and {311} peaks, respectively
Long scan	0°, 20°, 40° and 60°	{111}, {200}, {220}, {311} and {222} peaks

Table 4.1: The selection of ψ angles for different scans.

4.2.1. Experimental set-up for in-situ hydriding and kinetic analysis for the α-β phase transition

The observation of hydrogen absorption and desorption in Pd/Ti thin film were conducted by collecting diffraction XRD profiles during hydrogen loading/deloading performed at room temperature in a custom-made sample holder holder. During hydrogen loading in H_2/N_2 gas, the diffraction patterns of a scan with θ ranges from 43° to 49° covering both of the α and β peaks of the {111} planes were collected until the "quasi-equilibrium" point (the point while the phase transition got "locked in" [21]) was reached whether the α-β phase transition was completed or not. In this work, two different ratio of H_2/N_2 gas ($p(H_2)$) were selected: 0.05 atm (same as the condition of the experiments performed by Verma et al. [18]) and 0.1 (higher $p(H_2)$, in the attempt to overcome the energy barrier of the α-β phase transition and observe the subsequent microstructural behavior as explained in section 3). The data was used to qualitatively analyze the absorbing kinetics, and these results will be discussed in section 5. All the short and long scans given in Table 4.1 were measured under continuous gas flow with the same condition as for the scan of the α-β phase transition. The stress state and microstructural behavior during H_2 absorbing will be discussed in section 5. After finishing the scans for H_2 loading condition, H_2 was deloading in N_2 until no hydrogen was remained in the Pd/Ti film. The completion of the β-α phase transition could also be confirmed by the same scan series as for the α-β phase transition. The results will also be discussed in section 5. Eventually, both of the short and long scans were performed again for the hydrogen deloading condition to see the corresponding stress state and microstrain of the cycle (will be discussed in section 5). Table 4.2 and 4.3 illustrates the measured H_2 loading and deloading cycles in this work. As shown in Table 4.2, one extra H_2 loading cycle at $p(H_2) = 0.05$ for both of the open (L23) and compact-structured (L6) Pd/Ti samples was conducted after loading at higher $p(H_2)$ to observe the corresponding H_2 absorbing properties, stress states and microstructural changes at H_2 loading condition.

$p(H_2)$	**Open-structured Pd/Ti film**	**Compact-structured Pd/Ti film**
0.05 atm	L21 and L23	L2, L5 and L6[a]
0.1 atm	L22	L4

Table 4.2: The measured H_2 loading cycles (represented by L with the cycle number of the sample) for the open and compact-structured Pd/Ti films at different $p(H_2)$. a: The data for all the measurements of L3 and parts of the measurements of L2 (ψ = 20°, 40° and 60° for long scans) could not be collected due to the occurrence of technical problems of the equipment.

$p(H_2)$	**Open-structured Pd/Ti**	**Compact-structured Pd/Ti**
0 atm (loading at 0.05 atm)	D21[b]	D5[ab]
0 atm (loading at 0.1 atm)	D22	D4

Table 4.3: The measured H_2 deloading cycles (represented by D with the cycle number of the sample) for open and compact-structured Pd/Ti with different H_2 loading condition at the hydrogen loading stage. a: The data for all the measurements of D2 could not be collected due to the occurrence of technical problems of the equipment. b: D23 and D6 were not performed due to the time limitation of this work.

4.2.2. Macrostress measurements

To determine the stress states of the Pd/Ti film samples, conventional $\sin^2\psi$ method (illustrated by Equation 4.1 and 4.2) was used [29]. In the equations, $\epsilon_{\phi\psi}^{hkl}$ represents the mechanical strain for assigned ϕ (rotation angle illustrated in Figure 4.2 and 4.3) and ψ at certain hkl planes which can be calculated by the difference between the final interplanar distance ($d_{\phi\psi}^{hkl}$) and strain-free interplanar distance (d_0) divided by d_0. σ_{11} and σ_{22} are the principal stress at 1 and 2 direction illustrated in Figure 4.2. S_1^{hkl} and $\frac{1}{2}S_2^{hkl}$ are the elastic constants which the selection of the values will be discussed in the later part of this section.

$$\epsilon_{\phi\psi}^{hkl} = \frac{d_{\phi\psi}^{hkl} - d_0}{d_0} = \frac{1}{2}S_2^{hkl}.\sigma_\phi.\sin^2\psi + S_1^{hkl}(\sigma_{11} + \sigma_{22}). \tag{4.1}$$

where the in-plane stress (σ_ϕ) to be measured is equal to:

$$\sigma_\phi = \cos^2\phi(\sigma_{11})^2 + \sin^2\phi(\sigma_{22}). \tag{4.2}$$

From the texture measurements done by Verma et al. [18], it has been confirmed that rotational symmetry exists for the Pd/Ti samples. Thus, the rotation angle (ϕ) was fixed for all the measurements, and the value of in-plane stress will be represented by $\sigma_{//}$ instead of σ_ϕ in the rest parts of this work. However, in addition to the crystallographic texture, it was also noted that macroscopic anisotropy has to be taken into consideration for the columnar-structured Pd thin films deposited by magnetron sputtering. The existence of the macroscopic anisotropy for thin films is owing to the surface anisotropy which the crystallites adjacent to the surface has no neighboring crystallites on top of the direction perpendicular to the surface (unlike bulk which each crystallite is surrounded by neighboring crystallites in all 3 dimensions), thus, interactions between the crystallites located at the surface are not equivalent for all directions [30]. To tackle the issue of macroscopic anisotropy, single crystal analysis [31] was utilized to only analyze the crystallites with {111} planes parallel to the film surface. The information of those crystallites can be collected by analyzing the {311} peaks at $\psi = 29.5°$ and $58.5°$ which are the angles between {111} and {311} planes [18]. In this research, the reflection of the {311} peaks at around $\psi = 29.5°$ ($\psi = 26.57°$ and $33.21°$ from the short scans listed in Table 4.1) and $\psi = 58.5°$ ($\psi = 60°$ from the long scan listed in Table 4.1) were taken to calculate the stress state of the Pd/Ti film samples.

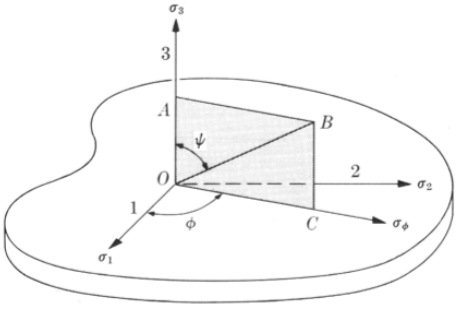

Figure 4.2: A schematic drawing of stress states at the surface of a body bi-axially stressed while σ_1 and $\sigma_2 \neq 0$ and $\sigma_3 = 0$. The in-plane stress to be measured is represented by σ_ϕ within the surface plane. Ref: [32]

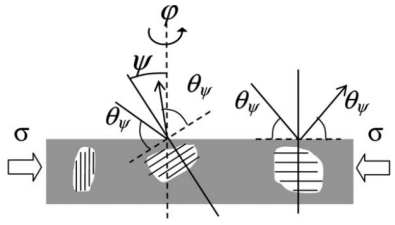

Figure 4.3: An illustration of different interplanar distances induced by the same compressive stress (σ) due to the different sample orientations. The data of the interplanar distances from different sample orientations can be collected by tilting the sample to a certain angle (ψ) to meet Bragg's condition and generate diffraction peaks. Ref: [29]

In this work, the interplanar distance of {311} planes (represented by $d_{\phi\psi}^{hkl}$ in Equation 4.1 where hkl = 311) was calculated by the peak positions of the {311} peaks fitted by Voigt function (will be explained in 4.2.3). Meanwhile, referred to the work done by Verma et al.[18], the Neerfeld-Hill average values [31] of the X-ray elastic constants: S_1^{hkl} and $\frac{1}{2}S_2^{hkl}$ (see Equation 4.1) were taken as -3.25 and 11.49 TPa^{-1} for Pd and -3.28 and 11.60 TPa^{-1} for $PdH_{0.66}$, respectively at room temperature, which were calculated from Pd single crystal elastic constants [33]. With known d_0 and $\frac{1}{2}S_2^{311}$, the in-plane stress ($\sigma_{//}$) parallel to the Pd/Ti film surface can be determined by the slope of the straight line fitted by the $d_{\phi\psi}^{311}$ - $\sin^2\psi$ plot according to Equation 4.1. The uncertainty of the stress value was evaluated based on the uncertainty of the slope. The results will be given and discussed in section 5.

4.2.3. XRD line-broadening analysis for microstructure characterization

In this work, line-broadening analysis of X-ray diffraction profile using the integral breadth of the peaks was utilized to understand the deformation mechanism with regard to defect parameters. The crystallite size and lattice microstrain induced by dislocation emissions were estimated [18] [34]. The integral breadth of the measured peak profile after $K_{\alpha 2}$ stripping was fitted by using the package of least-squares multi-peak fitting performed in Igor Pro [35]. Within the package, Voigt function (consist of Gaussian and Cauchy components arisen from microstrain and crystallite size, respectively [36] [37]) was used. A linear background was selected since the overlapping area of the peak was found to be properly fitted. The shape factor was fixed to be 1 which means that the ratio between the width of the line profile at half the maximum intensity (FWHM) and integral breadth (β) was fixed (approximately 0.71). This measurement was taken to avoid the occurrence of inappropriate fitting shape (errors) especially for low-intensity peaks. Since this analysis was used to qualitatively observe the microstructural evolution of the Pd/Ti thin films after H_2 (de)sorption at different p(H_2) instead of quantitatively determining the absolute dislocation density (microstrain) and crystallite size of the films, it was expected that the results were not significantly affected by the fixed shape factor.

The selection of the peaks for the long scans (shown in Table 4.1) at different loading/deloading cycles to be analyzed is illustrated in Table 4.4. As shown in the Table 4.4, most of the {220} peaks were not selected since the reflections of the peaks were found to be interfered by the Si{400} reflection induced by the Si/SiO_2 substrate [18] (especially at $\psi = 0°$ and 20°). Some of the other peaks were found to be overlapping with the substrate-induced reflection (bump). Thus, as indicated in Table 4.4, some of the peaks were chosen to be fitted together with the bump (fitted by Gaussian function to represent the characteristic of the broad Si induced-reflection). Furthermore, the background signal was found to be non-linear for some of the ψ angles. Hence, some of the peaks (which were confirmed that the reflections did not overlap with each other) were fitted solely by shrinking the range of 2θ to obtain the results with more accurate background signal. Some of the {200} and {222} peaks were discarded due to the lack of signal ({200} peaks for $\psi = 0°$ at L4, D4, L5, D5 and L6; {222} peaks for $\psi = 20°$ at D4, D5 and L6), or the severe interference from the substrate-induced bump (the rest of the non-selected peaks). In order to use the information of at least three peaks for the analysis, some of the {222} peaks are found to be able to be replaced by the {220} peaks (for $\psi = 40°$ and 60°) which were found not overlapping with Si-induced reflection.

In this research, NIST Standard Reference Material LaB6 (SRM660a) [18] was used as the reference specimen placed on a (510) Si single-crystal substrate to determine the instrumental profile in an analytical way. In this case, the broadening is expressed in degrees (2θ), and the profile parameters used and measured are represented by FWHM and integral breadth (β). As illustrated in Equation 4.3, the instrumental broadening ($\Delta 2\theta_i$) consists of spectral broadening ($\Delta 2\theta_s$) and geometrical broadening ($\Delta 2\theta_g$). The spectral broadening ($\Delta 2\theta_s$) can be derived from the differentiation of Bragg's law [38] as shown in Equation 4.4, in which $\Delta\lambda$ is the spectral width of the used wavelength (λ) expressed in eV or nm. Meanwhile, it was reported that the effect of geometric aberrations to the line profile of diffractometers equipped with parallel beam is less than non-parallel equipped ones, and the systematic errors owing to specimen displacement, transparency and surface roughness were found to be insignificant [39]. Hence, with less effect on the instrumental broadening, the geometrical broadening ($\Delta 2\theta_g$) was assumed to be a constant in Equation 4.5 in this case. Subsequently, with known measured angles (2θ ranges from 23° to 160°) and the corresponding measured instrumental broadening values ($\Delta 2\theta_i$, represented by FWHM and β, respectively), a straight line can be deduced in a $\Delta 2\theta_i$-$\tan\theta$ plot with slope = $2\Delta\lambda/\lambda$ and intersection = $\Delta 2\theta_g$ (see Equation 4.5). By using the analytical function using FWHM as profile parameters, the spectral width ($\Delta\lambda$) derived from the slope is calculated to be 0.476 mÅ which was found to match well with the value of $CoK_{\alpha 1}$ (0.47 mÅ) from the emission profile of Topas [40]. Thus, it could be concluded that the analytical function is applicable to obtain the instrumental broadening profile for the corresponding diffraction angle.

In this work, the slope and intersection of the measured FWHM profile were calculated to be 0.0305 and 0.2866, respectively. For the measured β profile, the slope and intersection were calculated to be 0.0388 and 0.3081, respectively. The standard deviation of the measured FWHM and β profile for the instrumental broadening was taken to be 0.01. It was also found that the slope is nearly the same for different ψ angles (0° and 70°), and there is only a slight increase (less than 2 %) for the intersection from $\psi = 0°$ to 70° which was found to be negligible for the interpretation of the results. Hence, the same values of the slope and intersection were taken for the instrumental broadening profile at different ψ angles.

$$\Delta 2\theta_i = \Delta 2\theta_s + \Delta 2\theta_g \tag{4.3}$$

$$\Delta\lambda/\lambda = \Delta\theta_s/\tan\theta \rightarrow \Delta 2\theta_s = 2\tan\theta.\Delta\lambda/\lambda \tag{4.4}$$

$$\Delta 2\theta_i = 2\tan\theta.\Delta\lambda/\lambda + \Delta 2\theta_g \tag{4.5}$$

The final retrieved XRD peak profile (broadening effect) is the result of the convolution of the instrumental broadening from the diffractometer and the broadening introduced by crystallographic imperfections (or microstrain) [18] [37]. In this research, the standard deviation of the measured peak profile (FWHM and β) was also taken to be 0.01, and the instrument-corrected final XRD peak broadening (β_{hkl}) was estimated using both Equation 4.6 and 4.7:

$$\beta_{hkl} = [(\beta_{hkl})^2_{measured} - (\beta_{hkl})^2_{instrumental}]^{1/2} \qquad \text{(Gaussian-like fitting)} \tag{4.6}$$

$$\beta_{hkl} = (\beta_{hkl})_{measured} - (\beta_{hkl})_{instrumental} \qquad \text{(Cauchy/Lorentzian-like fitting)} \tag{4.7}$$

since the shape of the involved measured peak profiles with shape factor fixed to be 1 which makes it close to Cauchy (Lorentzian)-like function [37]. On the other hand, the instrumental peak profile was found to be more Gaussian-like [18]. Thus, both of Equation 4.6 and 4.7 were decided to be used to calculate the broadening of the XRD profile. The results with and without the instrumental correction are going to be discussed in section 5.

In the rest of this thesis work, the final obtained broadening effect (β_{hkl}) will be replaced by the one in reciprocal space β^*_{hkl} as shown in Equation 4.8:

$$\beta^*_{hkl} = \beta_{hkl}\cos\theta/\lambda \tag{4.8}$$

In this work, it was assumed that the microstructural broadening effect is induced from both microstrain and crystallite size. Thus, the total broadening effect represented by the integral breadth of a Bragg peak can be derived by the summation of these two components. Furthermore, since there was found to be no effect of stacking and twinning faults in the measured peak profile [18], the contribution of the microstrain component to the line broadening could be solely assigned to dislocation emissions and evaluated by modified Williamson-Hall (mod-WH) method [18] [41] [42] illustrated by Equation 4.9. This method is used to tackle the anisotropic properties (strain fields) of dislocations by introducing the contrast factor (C_{hkl}) [43] [44] which depends on the types, densities, and arrangements of the present dislocations, as well as the orientation distribution of the dislocations with respect to the diffraction vector.

$$\beta^*_{hkl} = K/ < D > +(\pi M^2 b^2/2)^{1/2}[(h^2+k^2+l^2)/a^2]^{1/2}\rho^{1/2}C^{1/2}_{hkl} \tag{4.9}$$

where K is a constant (taken as 1 in this work), <D> (nm) is the average crystallite size (here the direction is perpendicular to the tilting angles (ψ) [18]), M is a constant to describe the arrangement of the dislocations (here is taken as 1 [18]), ρ is the dislocation density (m^{-2}), be is the Burgers vector, hkl is the diffractive plane, and a is the lattice constant. Further details of the calculation of the contrast factors (C_{hkl}) is presented in the previous work done by Verma et al. [18]. In this work, randomly oriented pure screw dislocations of the {111}, a/2<110> slip system was assumed to be dominant among all the possible involved slip systems (explained in the same report done by Verma et al.) since the best fit was attained for this slip system for nearly all the XRD line-broadening profiles. The results of the line-broadening profile of the Pd/Ti samples will be discussed in section 5.

ψ **angle (L21)**	{111} peak	{200} peak	{220} peak	{311} peak	{222} peak
0°	$\surd$	$\surd$		$\surd^{b}$	$\surd^{b}$
20°	$\surd^{a}$	$\surd^{a}$		$\surd^{a}$	$\surd^{a}$
40°	$\surd$	$\surd$	$\surd^{b}$	$\surd^{b}$	
60°	$\surd$	$\surd$		$\surd^{b}$	$\surd^{b}$
ψ **angle (D21)**	{111} peak	{200} peak	{220} peak	{311} peak	{222} peak
0°	$\surd^{c}$	$\surd^{c}$		$\surd^{c}$	
20°	$\surd^{b}$	$\surd^{b}$		$\surd$	$\surd$
40°	$\surd^{a}$	$\surd^{a}$	$\surd^{b}$	$\surd^{b}$	
60°	$\surd$	$\surd$		$\surd^{b}$	$\surd^{b}$
ψ **angle (L22)**	{111} peak	{200} peak	{220} peak	{311} peak	{222} peak
0°	$\surd$	$\surd$		$\surd^{b}$	$\surd^{b}$
20°	$\surd^{a}$	$\surd^{a}$		$\surd$	$\surd$
40°	$\surd$	$\surd$	$\surd^{b}$	$\surd^{b}$	
60°	$\surd$	$\surd$		$\surd^{b}$	$\surd^{b}$
ψ **angle (D22)**	{111} peak	{200} peak	{220} peak	{311} peak	{222} peak
0°	$\surd^{a}$	$\surd^{a}$		$\surd$	$\surd$
20°	$\surd^{a}$	$\surd^{a}$		$\surd$	$\surd$
40°	$\surd$	$\surd$	$\surd^{b}$	$\surd^{b}$	
60°	$\surd$	$\surd$	$\surd^{b}$	$\surd^{b}$	
ψ **angle (L23)**	{111} peak	{200} peak	{220} peak	{311} peak	{222} peak
0°	$\surd$	$\surd$		$\surd^{b}$	$\surd^{b}$
20°	$\surd^{b}$	$\surd^{b}$		$\surd^{a}$	$\surd^{a}$
40°	$\surd$	$\surd$	$\surd^{b}$	$\surd^{b}$	
60°	$\surd$	$\surd$		$\surd$	$\surd$
ψ **angle (L2)**	{111} peak	{200} peak	{220} peak	{311} peak	{222} peak
0°	$\surd^{a}$			$\surd^{b}$	$\surd^{b}$
ψ **angle (L4)**	{111} peak	{200} peak	{220} peak	{311} peak	{222} peak
0°	$\surd^{a}$			$\surd^{b}$	$\surd^{b}$
20°	$\surd$	$\surd$		$\surd^{a}$	$\surd^{a}$
40°	$\surd^{a}$	$\surd^{a}$	$\surd^{a}$	$\surd$	
60°	$\surd$	$\surd$		$\surd^{a}$	
ψ **angle (D4)**	{111} peak	{200} peak	{220} peak	{311} peak	{222} peak
0°	$\surd^{a}$			$\surd^{a}$	$\surd^{a}$
20°	$\surd^{b}$	$\surd^{b}$		$\surd^{a}$	
40°	$\surd$	$\surd$	$\surd^{a}$		
60°	$\surd$	$\surd$		$\surd^{b}$	
ψ **angle (L5)**	{111} peak	{200} peak	{220} peak	{311} peak	{222} peak
0°	$\surd^{a}$			$\surd$	$\surd$
20°	$\surd$	$\surd$		$\surd^{a}$	$\surd^{a}$
40°	$\surd^{a}$	$\surd^{a}$	$\surd^{a}$	$\surd^{b}$	
60°	$\surd$	$\surd$	$\surd^{a}$	$\surd^{b}$	
ψ **angle (D5)**	{111} peak	{200} peak	{220} peak	{311} peak	{222} peak
0°	$\surd^{a}$			$\surd^{a}$	$\surd^{a}$
20°	$\surd^{b}$	$\surd^{b}$		$\surd^{a}$	
40°	$\surd$	$\surd$		$\surd^{b}$	$\surd^{b}$
60°	$\surd$	$\surd$		$\surd^{b}$	
ψ **angle (L6)**	{111} peak	{200} peak	{220} peak	{311} peak	{222} peak
0°	$\surd^{a}$			$\surd$	$\surd$
20°	$\surd^{a}$	$\surd^{a}$		$\surd^{a}$	
40°	$\surd^{a}$	$\surd^{a}$	$\surd^{a}$	$\surd^{b}$	
60°	$\surd$	$\surd$	$\surd^{b}$	$\surd^{b}$	

Table 4.4: The selection of peaks (filled by the check mark) for different cycle number and ψ angles. The original fitting method (represented by the check mark without any signs) is to fit {111} and {200} peaks together and fit {311} and {222} peaks together, respectively. a: The peak was fitted solely. b: The peak was fitted with the Si/SiO_2 substrate-induced reflection. c: The data is retrieved from short scans instead of long scans for better results.

5. Results and discussion

In this section, the sample history including the stress states, dislocation densities and average crystallite sizes of the open-structured Pd/Ti sample will be discussed firstly. Secondly, the qualitative kinetic analysis of both of the open and compact-structured Pd/Ti samples during H_2 absorption (at different $p(H_2)$)/desorption will be introduced. Thirdly, the stress analysis of the open and compact-structured Pd/Ti film at hydrogen loading (at different $p(H_2)$) and deloading condition will be illustrated. Last but not least, the results of the line-broadening analysis for the open and compact-structured Pd/Ti sample at different loading (at different $p(H_2)$) and deloading cycles will be explained.

5.1. The history of the stress states and dislocation densities of the selected open-structured Pd/Ti film

As explained in 4.1, the open-structured Pd/Ti thin film selected for this research has undergone 20 H_2 loading and deloading cycle. Therefore, it is important that the actual condition of the Pd/Ti sample is analyzed before we performed the new measurements for this work. The following sections are going to illustrate and discuss the results of the previous stress states and dislocation densities at the 1_{st}, 5_{th}, 10_{th}, 16_{th} and 20_{th} hydrogen (de)loading cycle that were previously done [45].

5.1.1. The stress states of the selected open-structured Pd/Ti film at previous H_2 loading and deloading cycles

The XRD measurements for the previous 20 H_2 loading cycles were performed on the same equipment and procedure as mentioned in 4.2.1 at room temperature with $p(H_2) = 0.05$ atm. In the meantime, the short scans at $\psi = 0°$, 10°, 20°, 30°, 40°, 50°, 60°, 70° and 75° covering the same peaks as shown in Table 4.1 were performed and the peaks were fitted with a linear background using the Bruker - EVA software [18]. However, as explained in 4.2.2, only the measurements at $\psi = 30°$ (near 29.5°) and 60° (near 58.5°) were taken to be analyzed in this research. Since only two data points could collected for the calculation of the slope to determine the in-plane stress by the conventional $\sin^2\psi$ method introduced in 4.2.2, the uncertainty in the stress value could not be determined. Nevertheless, it is expected that this stress analysis could still provide a good insight regarding the previous stress conditions of the sample.

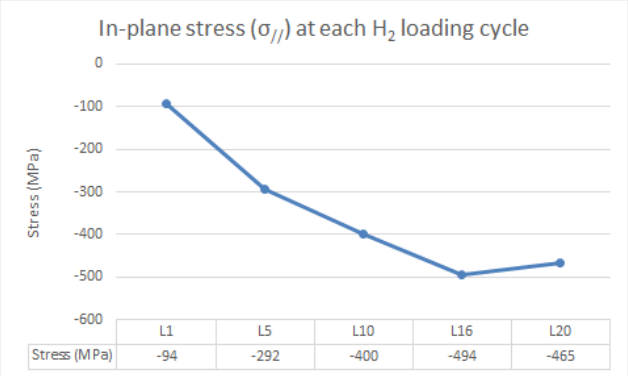

Figure 5.1: The trend of the in-plane stress states ($\sigma_{//}$) during H_2 loading cycles.

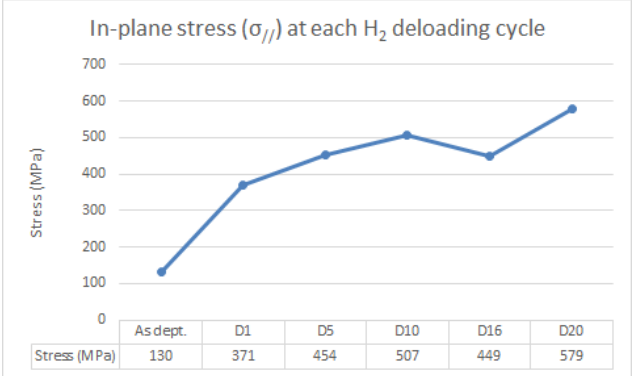

Figure 5.2: The trend of the in-plane stress states ($\sigma_{//}$) during H_2 deloading cycles including the original as-deposited condition (illustrated as "As dept." in the figure).

From Figure 5.1, it is clear that compressive stress (negative values of in-plane stress) increased almost linearly as the H_2 loading cycle number increased until the 16_{th} H_2 cycle. Tensile stress also built up as the cycle number increased for H_2 deloading as depicted in Figure 5.2. These results suggest that there is a significant difference between the original and final stress state after undergoing 20 H_2 loading and deloading cycles. Compared with the results provided by Verma et al. after 1 H_2 loading/deloading cycle (L1: -88 ± 16 MPa; D1: 380 ±

3 MPa) [18], it is clear that residual stress increases dramatically for the Pd/Ti film sample after H_2 loading and deloading cycles. This result (especially for H_2 loading condition) may justify the selection of the sample (explained in 4.1) as the energy barrier for hydrogen absorption could be increased by the increasing compressive stress already leading to the incomplete α-β phase transition at L20 ($p(H_2) = 0.05$ atm) for the open Pd/Ti sample used in this research (see Figure 8.3 in Appendix).

5.1.2. The dislocation densities and average crystallite sizes of the selected open-structured Pd/Ti film at previous H_2 loading and deloading cycles

From the same XRD measurement as in 5.1.1, the data of the long scan (covering all the diffractive peaks) at $\psi = 0°$ was used to conduct the line-broadening analysis. The same methodology was performed as same as 4.2.3, and the results of the dislocation densities and average crystallite sizes at each H_2 loading cycle with the instrumental correction sq_f (referred to Equation 4.3) are given in Figure 5.3 and 5.4. It should be noticed that the same trend could be attained by the line-broadening analysis with (L_f and sq_f, see 4.2.3) or without (h) correction from the instrumental profile. Hence, the results of sq_f were selected to be qualitatively discussed in this section. The statistic error of 3 standard deviations (3 σ) is illustrated by the error bar for sq_f.

In Figure 5.3, it is clear that a slightly downward trend of dislocation density (ρ) was obtained (excluding L16). Combined with the results of the stress states provided in Figure 5.1, it might suggest that the relaxation of the α-β phase transition-induced compressive stress by dislocations at H_2 loading condition (discussed in 3.1) become harder as the hydrogen loading cycle number increases. As a result, the compressive stress was found to increase, and the emission of dislocations slightly decreases. In terms of the average crystallite size (D) of the open Pd/Ti sample, no clear trend was observed. The average crystallite size of the Pd/Ti sample at L20 was found to be nearly the same as L1.

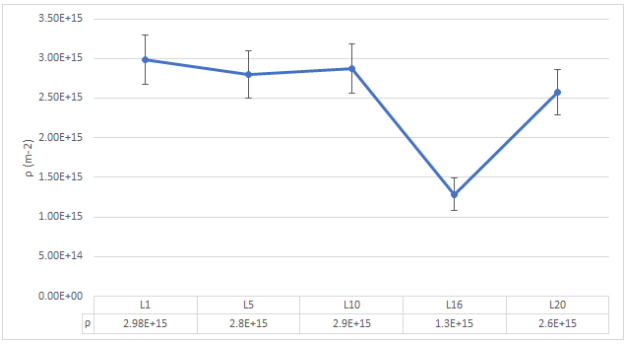

Figure 5.3: The trend of the dislocation densities (ρ) during H_2 loading cycles derived from the line-broadening analysis with the instrumental correction for Gaussian-like fitting (sq_f) as explained in 4.2.3. The statistic error of 3 standard deviations (3 σ) is illustrated by the error bar.

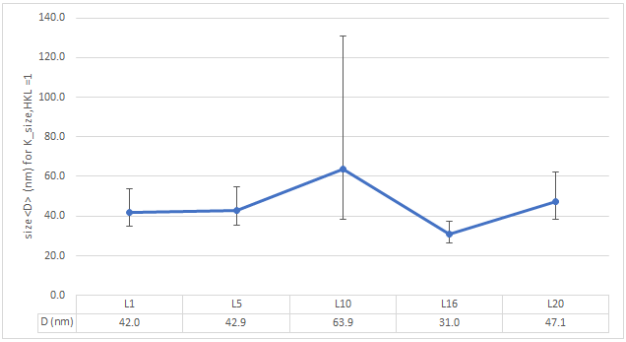

Figure 5.4: The trend of the average crystallite size (D) during H_2 loading cycles derived from the line-broadening analysis with the instrumental correction for Gaussian-like fitting (sq_f) as explained in 4.2.3. The statistic error of 3 standard deviations (3 σ) is illustrated by the error bar.

The changes of ρ and D during the H_2 deloading from D1 to D20 are also provided in Figure 5.5 and 5.6. The

measured XRD profile of the long scan for D10 was found to be difficult to be properly fitted because of the severe interference from background signal or Si/SiO_2-induced bump. Thus, excluding the data point of D10, it could be noticed that no significant changes for both ρ and D could be identified throughout the whole H_2 deloading cycle history.

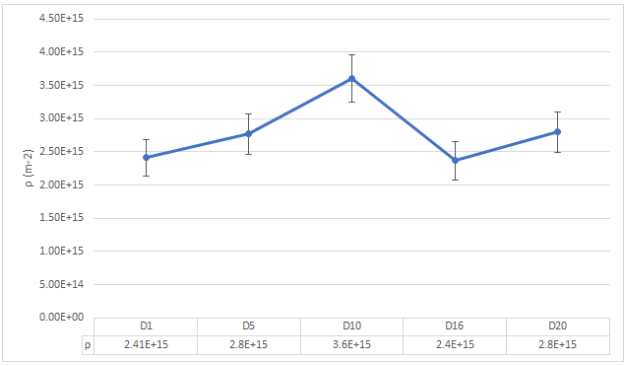

Figure 5.5: The trend of the dislocation densities (ρ) during H_2 deloading cycles derived from the line-broadening analysis with the instrumental correction for Gaussian-like fitting (sq_f). The statistic error of 3 standard deviations (3 σ) is illustrated by the error bar.

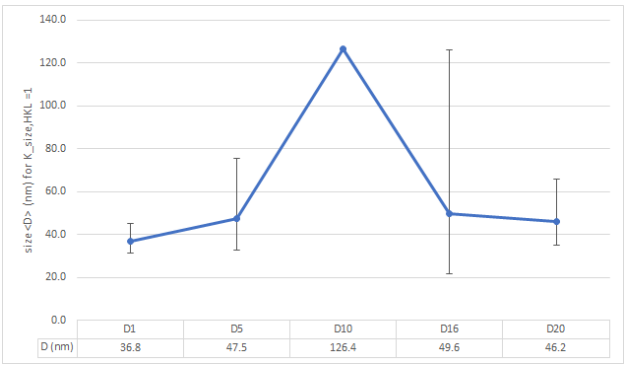

Figure 5.6: The trend of the average crystallite size (D) during H_2 deloading cycles derived from the line-broadening analysis with the instrumental correction for Gaussian-like fitting (sq_f). The statistic error of 3 standard deviations (3 σ) is illustrated by the error bar for $sq\_f(D)$. The error bar of D10 for $sq\_f(D)$ could not be retrieved since the data could not be properly fitted.

5.2. Kinetic analysis for the α-β phase transition during H_2 absorption at different p(H_2) and the β-α phase transition during H_2 desorption in N_2 for open and compact-structured Pd/Ti thin films

The kinetic analysis was performed by collecting the data of {111} reflections every hour and fitting it by using Voigt function introduced in 4.2.3 to observe the H_2 absorbing properties (α-β phase transition) at different p(H_2) and H_2 desorbing properties (β-α phase transition) at pure N_2 for both the open and compact-structured Pd/Ti films. The transformed phase fraction was determined by the fitted peak area of both the α (A_α) and β (A_β) phase [46] as shown in Equation 5.1 and 5.2. Meanwhile, the integral breadths of both of the {111} α and β peaks at $\psi = 0°$ during the hydriding/dehydriding process are also provided in this section. Despite that the integral breadth of the {111} peaks could only provide the information of microstrain occurred at the {111} planes (instead of dislocation density (ρ) which requires the peak information of at least three different {hkl} planes [18] to be reliable), the trend of the integral breadths for both of the phases during the measurements was found to be an important indicator of the microstructural behaviour for the Pd/Ti samples. This will be explained separately for the open and compact-structured Pd/Ti films. Since the trend of the integral breadth changes of the {111} peaks was found to be independent of the instrumental-broadening effect discussed in 4.2.3, only the fitted peak profiles without instrumental correction will be discussed in this section.

$$transformed\ phase\ fraction\ during\ H_2\ absorption = A_\beta/(A_\alpha + A_\beta) \tag{5.1}$$

$$transformed\ phase\ fraction\ during\ H_2\ desorption = A_\alpha/(A_\alpha + A_\beta) \tag{5.2}$$

5.2.1. Kinetic analysis for the open-structured Pd/Ti thin film during H_2 absorption

The data of L21 ($p(H_2) = 0.05$) and L22 ($p(H_2) = 0.1$) for the open-structured Pd/Ti film was used to compare the differences between the H_2 absorbing properties at different H_2 loading conditions. Figure 5.7 illustrates the α-β phase transformed fraction as a function of time at L21 ($p(H_2) = 0.05$ atm). As shown in the figure, the "quasi-equilibrium" point was reached after 1 hour which the phase transition was approximately 90% completed. This indicates that the phase transition in the open-structrued Pd/Ti thin film sample can not be completed at $p(H_2) = 0.05$ atm after 20 H_2 loading and deloading cycles. By contrast, the phase transition was found to be 100% completed in less than 3 minutes during L22 when a higher H_2 partial pressure ($p(H_2) = 0.1$ atm) was applied for the same sample. Thus, it could be concluded that the applied $p(H_2)$ is high enough to fully overcome the energy barrier of the α-β phase transition for the open Pd/Ti film sample. The figure of α-β phase transformed fraction versus time at L22 could not be provided since the transition was completed in less than the time period of 1 scan (roughly 2.5 minutes).

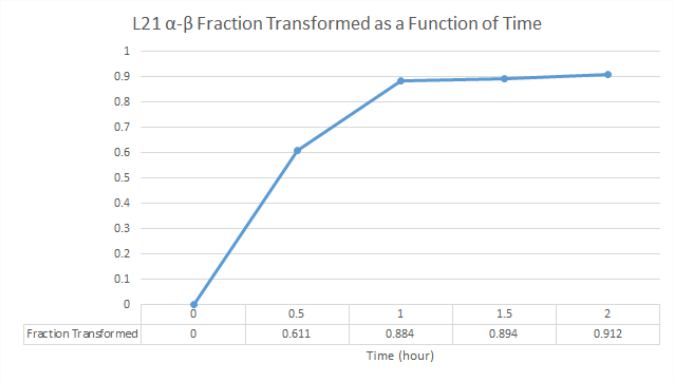

Figure 5.7: The α-β phase transformed fraction as a function of time during the H_2 absorption at L21 for the open-structured Pd/Ti sample.

The integral breadths of the {111} peaks for both of the α and β phases during the transition at L21 are illustrated in Figure 5.8. From the figure, it is clear that the integral breadth steadily increases until roughly 1.5 hours and remains at a certain level afterwards. This might indicate that microstrain induced by dislocation emission was piled-up in the α phase of {111} planes which matches the results of the BCDI analysis done by A. Ulvestad and A. Yau [17]. On the other hand, the integral breadth of the β peak for the {111} planes slightly decreases during the hydriding which probably means that microstrain induced by dislocation emission does not build up (or to a lesser extent) in the β phase.

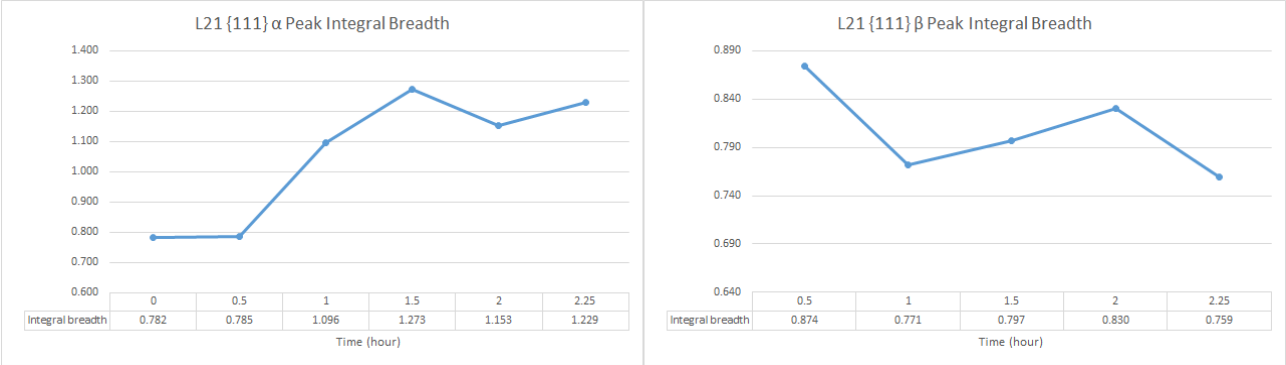

Figure 5.8: The integral breadths of the {111} peaks of both α (left figure) and β (right figure) phases during the H_2 absorption at L21 for the open-structured Pd/Ti sample. There was no β phase (peak) at the start of the hydriding process.

After L22 that showed a complete α-β phase transition at applied $p(H_2) = 0.1$ atm, a next loading, again at lower partial pressure (L23, $p(H_2) = 0.05$ atm) was performed. The H_2 absorbing properties were found to be different from L21 ($p(H_2) = 0.05$ atm) as depicted in Figure 5.9 and 5.10. The "quasi-equilibrium" phase was reached in 15 minutes which was much faster than for L21 (1 hour) at the same $p(H_2)$ also approximately 4% higher fraction was transformed. Meanwhile, unlike L21, it is hard to identify that microstrain was built-up at α or β phase. These results might be an indication that the stress state and microstructure of the open-structured Pd/Ti sample changed after applying the $p(H_2) = 0.1$ atm at L22, which will be further discussed in 5.3 and 5.4.

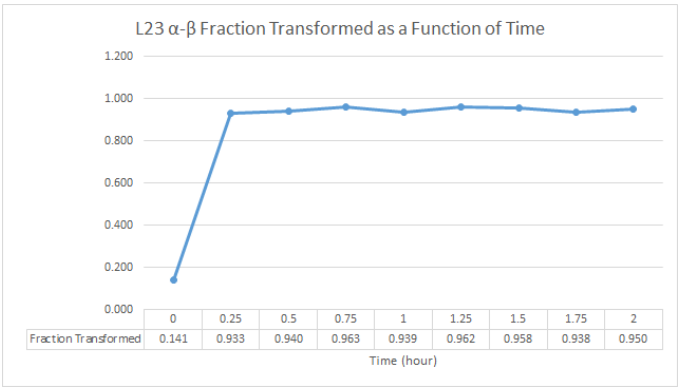

Figure 5.9: The α-β phase transformed fraction during the H_2 absorption at L23 for the open-structured Pd/Ti sample.

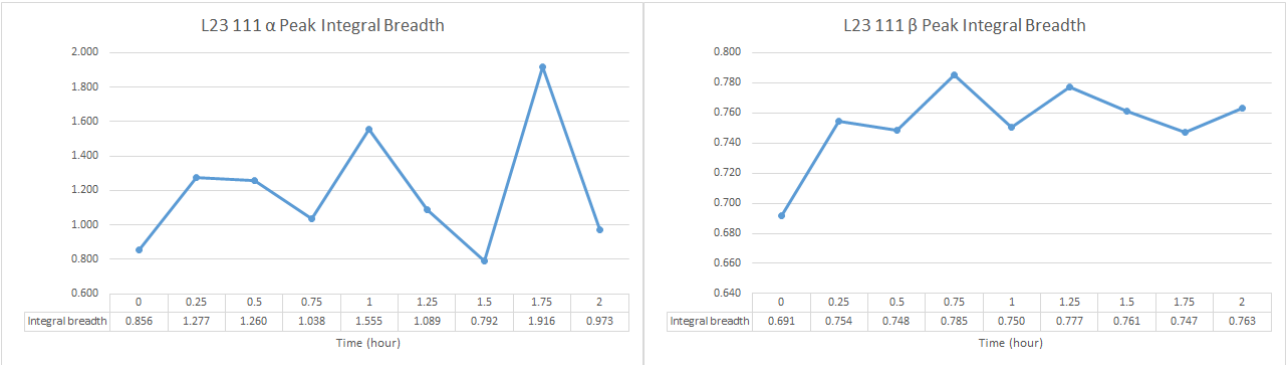

Figure 5.10: The integral breadths of the {111} peaks of both α (left figure) and β (right figure) phases during the H_2 absorption at L23 for the open-structured Pd/Ti sample.

5.2.2. Kinetic analysis for the compact-structured Pd/Ti thin film during H_2 absorption

The data of L2, L4, L5 and L6 was retrieved to compare of the differences between the H_2 absorbing properties at $p(H_2) = 0.05$ (L2, L5 and L6) and 0.1 atm (L4) for the compact-structured Pd/Ti sample. The results of L2, L5 and L6 will be discussed and followed by the results of L4.

Figure 5.11 compares the α-β phase transformed fraction as a function of time at L2, L5 and L6 with $p(H_2) = 0.05$ atm. From the figure, it could be observed that the "quasi-equilibrium" phase transformed fraction at L2 is roughly 92% which is quite similar to the open Pd/Ti sample at L21 with much slower hydrogen absorbing kinetic (time to reach the "quasi-equilibrium" point: approximately 5 hours). This result highlights the morphology of the Pd/Ti film strongly affects the uptake of hydrogen [18]. On the other hand, after undergoing 2 H_2 loading cycles (L3 at $p(H_2) = 0.05$ atm, L4 at $p(H_2) = 0.1$ atm), a significant decrease of the phase transformed fraction was observed (L5: 77%, L6: 81%) for the same Pd/Ti film with compact structure. Meanwhile, compared with L2, much slower kinetics (roughly 30 hours for both L5 and L6 to reach the "quasi-equilibrium" phase transition point) of H_2 absorption was identified as well. This observation might be an indicator that the Pd/Ti sample became more compact-structured as the hydrogen loading/deloading cycle number increased. Seemingly this further elevated the energy barrier and slowed down the kinetics of H_2 absorption. Further explanation will be given in 5.3 to validate this observation.

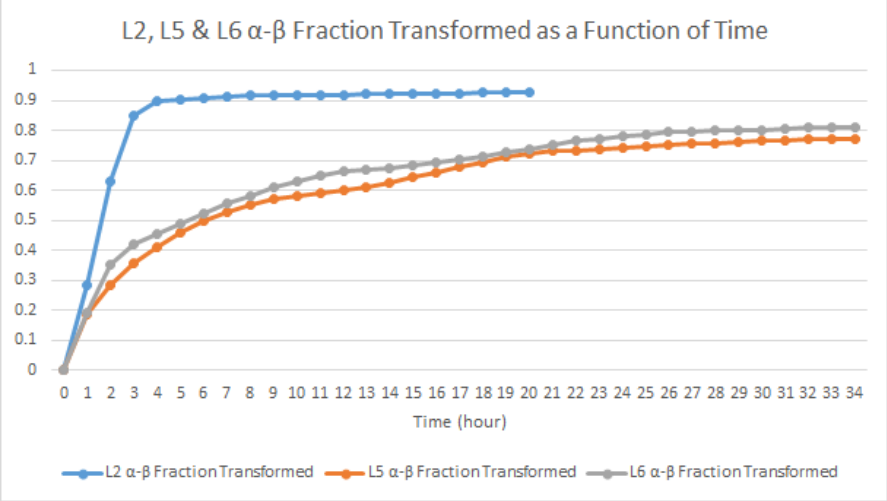

Figure 5.11: The α-β phase transformed fraction as a function of time during the H_2 absorption at L2, L5 and L6 for the compact-structured Pd/Ti sample.

Moreover, the integral breadths of the {111} peaks for the α and β phases during the transition at L2, L5 and L6 are depicted in Figure 5.12 and 5.13, respectively. From Figure 5.12, a steep upward trend of the integral breadth of the α peak could be recognized during L2 until the "quasi-equilibrium" transition state was reached, followed by a constant level of the breadth at roughly 0.9 nm^{-1}. By contrast, the integral breadth of the β peak during L2 (shown in Figure 5.13) decreased significantly during the phase transition and remained nearly as a constant after the maximum phase transformed fraction was reached. This is similar to the result of the open-structured Pd/Ti which might support the theory that microstrain induced by dislocation emission mainly piled-up at α phase [17]. Compared with L2, a steady linear increase of the breadth of α peak with much smaller slopes and values could be recognized during the whole hydriding process at L5 and L6. This might suggest that the microstrain induced by the emission of dislocations was restricted for the compacted-strcutured Pd/Ti film. This will be further discussed in 5.4. Regarding the integral breadth of the β peaks, the same trend could be seen for L5 and L6 as for L2 during the hydriding. This again supports that dislocations were probably not emitted at β phase.

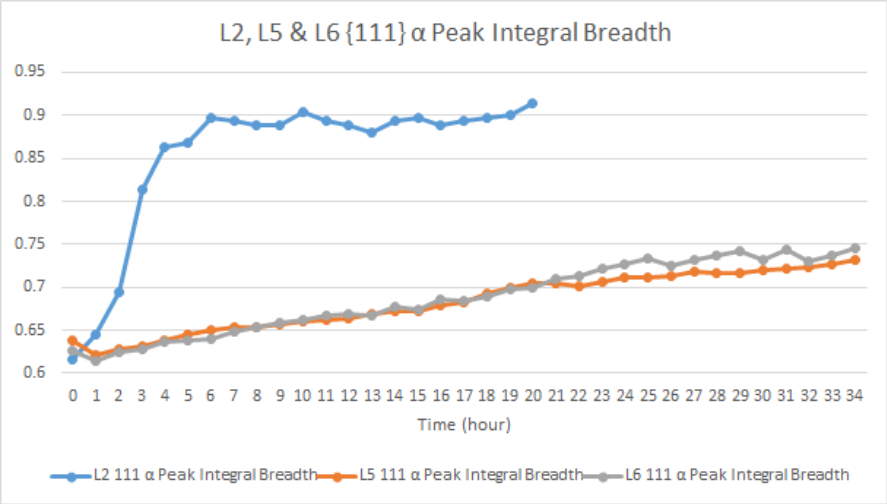

Figure 5.12: The changes of integral breadths of the {111} peak of the α phase during the H_2 absorption at L2, L5 and L6 for the compact-structured Pd/Ti sample.

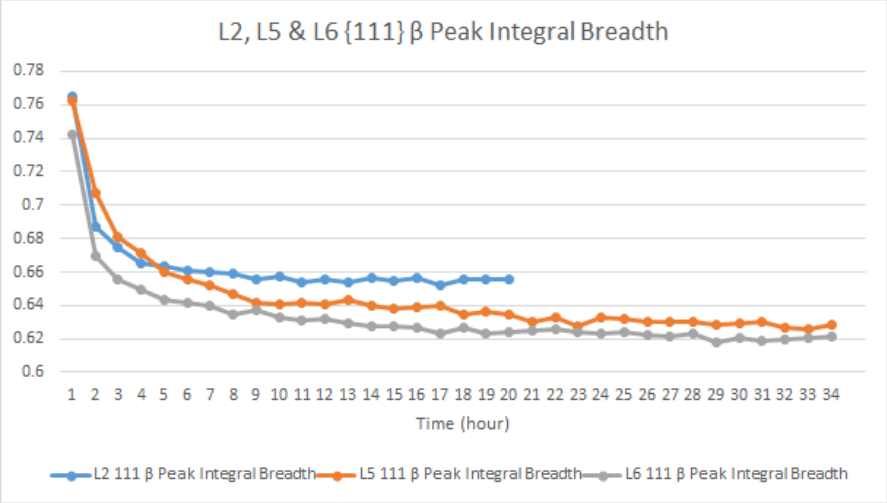

Figure 5.13: The changes of integral breadths of the {111} peak of the β phase during the H_2 absorption at L2, L5 and L6 for the compact-structured Pd/Ti sample.

In the attempt to fully overcome the energy barrier of the α-β phase transition for the compact-structured Pd/Ti thin film, higher H_2 partial pressure ($p(H_2) = 0.1$ atm) was applied at L4. The phase transformed fraction as a function of time during the hydriding period of L4 is given in Figure 5.14 which illustrates that the transition was 100% completed in less than two hours. This demonstrates that the applied $p(H_2)$ is sufficient enough to fully conquer the energy barrier of the phase transition for the compact-structured Pd/Ti sample with slower H_2 absorbing kinetics compared with L22 (less than 3 minutes, as explained in 5.2.1) for the open-structured Pd/Ti.

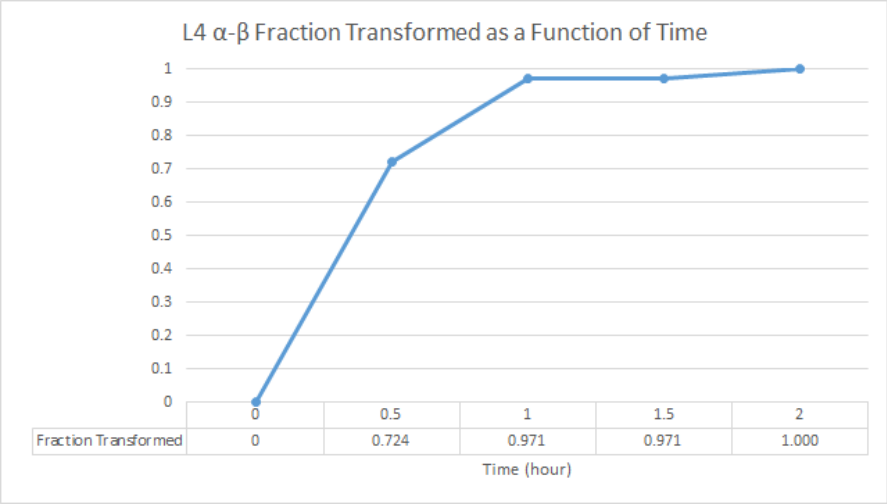

Figure 5.14: The α-β phase transformed fraction as a function of time during the H_2 absorption at L4 for the compact-structured Pd/Ti sample.

In terms of the integral breadth of the α peak, the same upward trend during L4 as L2, L5 and L6 (only comparing the part of linear growth until the "quasi-equilibrium" phase transition point was reached) with a steeper slope could be identified in Figure 5.15. This may imply that microstrain was built-up at α phase more rapidly at higher $p(H_2)$ for the compact-structured Pd/Ti sample. At the meantime, despite that the α phase was 100% transformed into β phase, the dislocation density of L4 at $\psi = 0°$ was also found to be significantly higher than L5 and L6 and slightly higher (within 1 standard deviation) than L2 at the same ψ angle, which will be further discussed in 5.4. For the evolution of the breadth for the β peak during L4, the same downward trend as L2, L5 and L6 was obtained which may support that dislocation mostly emits at α phase during the hydriding process regardless of applied $p(H_2)$.

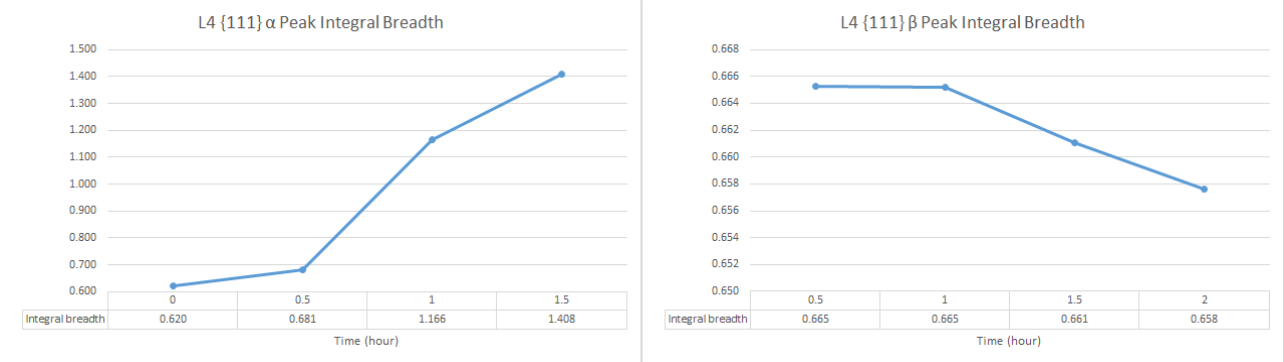

Figure 5.15: The integral breadths of the {111} peaks of both α (left figure) and β (right figure) phases during the H_2 absorption at L4 for the compact-structured Pd/Ti sample. There was no β phase (peak) at the start of the hydriding process, and there was no α phase remaining at the end of it.

5.2.3. Kinetic analysis for the open-structured Pd/Ti thin film during H_2 desorption after loading at different $p(H_2)$

In Figure 5.16, the β-α phase transformed fraction versus time during D22 (after L22 loading at $p(H_2) = 0.1$ atm) and D23 (after L23 loading at $p(H_2) = 0.05$ atm) was compared. It is obvious that the transition was completed more rapidly for the dehydriding process of D22 than D23. This might be owing to the less remaining dislocations of L22 than L23 (given in Figure 5.20) which could act as unoccupied trapping sites for hydrogen atoms to slow down the kinetics of desorption at D23 (will be explained in 5.2.4). In addition, the changes of the breadth of both {111} α and β peaks during D22 and D23 was given in Figure 5.17. In the figure, it could be seen that microstrain gradually built up at α phase during D22 but piled up at β phase during D23. This

might again be an implication that microstructural evolution occurred after experiencing high pressurization by hydrogen for the open-structured Pd/Ti sample.

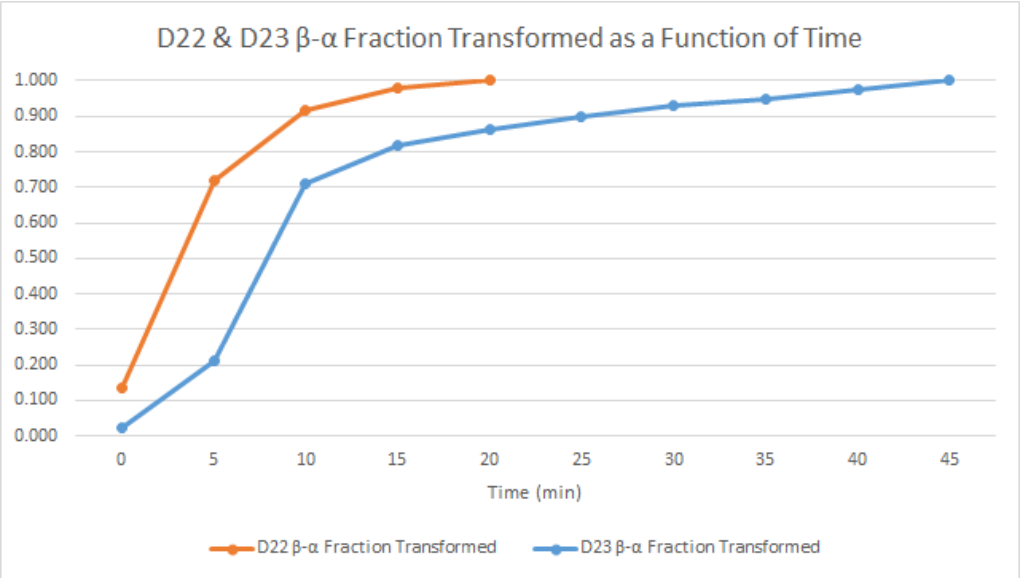

Figure 5.16: The β-α phase transformed fraction as a function of time during the H_2 absorption at D22 and D23 for the open-structured Pd/Ti sample. The data of D21 could not be collected due to technical problems.

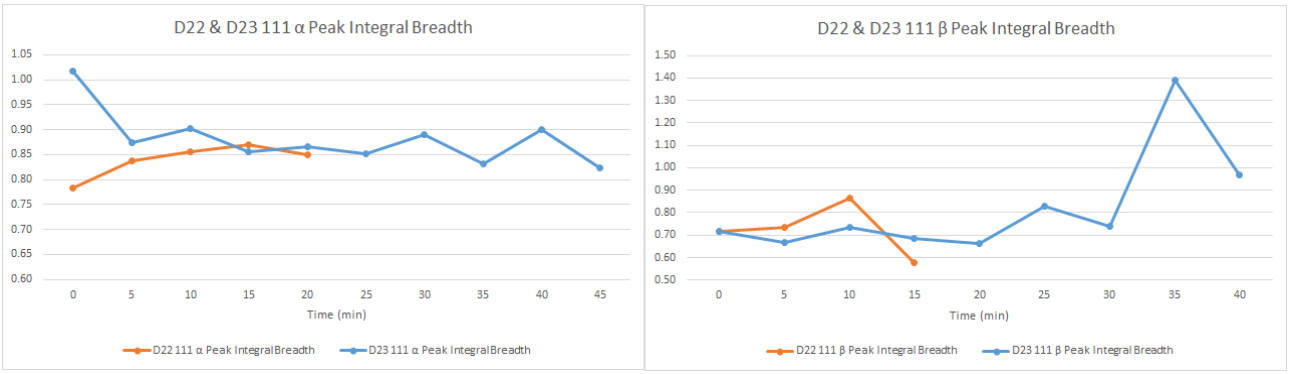

Figure 5.17: The integral breadths of the {111} peaks of both α (left figure) and β (right figure) phases during the H_2 absorption at D22 and D23 for the open-structured Pd/Ti sample. The data of D21 could not be collected due to technical problems.

5.2.4. Kinetic analysis for the compact-structured Pd/Ti thin films during H_2 desorption after loading at different p(H_2)

Figure 5.18 compares the results for the β-α phase transformed fraction as a function of time for the compact-structured Pd/Ti sample during the H_2 deloading process at D4 (after H_2 loading at p(H_2) = 0.1 atm), D5 (after H_2 loading at p(H_2) = 0.05 atm) and D6 (after H_2 loading at p(H_2) = 0.05 atm). From the figure, it could be recognized that the β-α phase transition of D4 was slightly slower than D5 and D6. This could be attributed to the higher tensile stress induced by the clamping effect [22], which will be further discussed in 5.3. In addition, dislocation emission might be another contributor to this result. Combined with Figure 5.28 which shows that the dislocation density at D4 is higher than D5 at $\psi = 0°$, this could be an indicator that more dislocations could act as the trapping sites for hydrogen atom to slightly slow the desorption kinetics at the beginning stage of D4 [15]. Moreover, this result might also be owing to the increasing number of grain boundaries acting as fast diffusion pathways [15] as H_2 loading/deloading cycle number increased. This could probably be supported by the smaller average crystallite size found at D5 than D4 (at $\psi = 0°$ illustrated in

Figure 5.29) since the reduction of grain size could introduce dislocation-accommodated grain boundaries [47]. As a result, the phase transition kinetic of D4 was slower (approximately 3.5 hours) than D5 (roughly 3 hours).

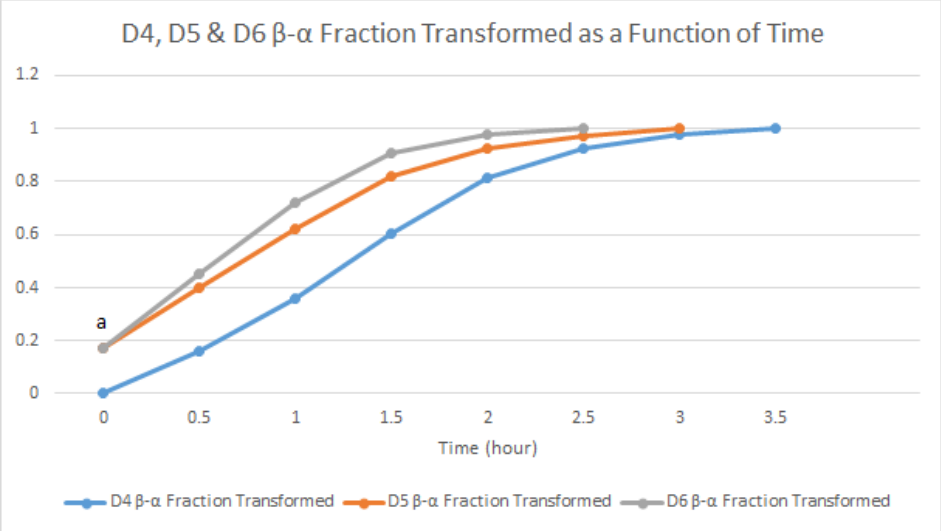

Figure 5.18: The β-α phase transformed fraction versus time during the H_2 desorption at D4, D5 and D6 for the compact-structured Pd/Ti sample. a: The transformed fraction measured at "0 hour" was not zero since the measurement was found to be roughly 30 seconds to 1 minute delayed. Thus, the partial β-α phase transition already started at "0 hour" during D5 and D6.

Meanwhile, after loading at $p(H_2) = 0.05$ atm at L5 and L6, the kinetics of H_2 desorption at D5 and D6 (less than 3 hours to complete the transition) is dramatically faster than H_2 absorption at L5 and L6 for the compact-structured Pd/Ti sample (20 to 30 hours to reach the "quasi-equilibrium" phase transition, see Figure 5.11). The slower kinetics of H_2 absorption at L5 and L6 could be again attributed to dislocations acting as unoccupied trapping sites for H atoms until a certain amount of the sites were occupied by the trapped H atoms during the H_2 absorption [15]. By contrast, since most of the trapping sites were already occupied by the hydrogen atoms during H_2 absorption, the free hydrogen atoms were not easily trapped at the H atoms-occupied trapping sites at the beginning stage of the H_2 desorption [15], which is the reason why the H_2 desorption is generally faster than H_2 absorption. However, after loading at $p(H_2) = 0.1$ atm at L4 for the same sample, it was found that the H_2 desorbing kinetics at D4 (roughly 3.5 hours as indicated in Figure 5.18) is slower than the H_2 absorbing kinetics L4 (less than 2 hours, see Figure 5.14). This could again be an indicator that the energy barrier could be fully overcome by the applied $p(H_2) = 0.1$ atm during H_2 absorption, thus, the α-β phase transition would not get locked in at the "quasi-equilibrium point" which significantly accelerated the kinetics of H_2 absorption at L4.

The results of the integral breadth of the {111} peaks for both α and β phases during H_2 desorption are provided in Figure 5.19. As depicted in the figure, it is clear that the trends of the breadth for both of the phases are completely the opposite of the trends for H_2 absorption. For H_2 desorption, a downward trend was found for the α peak at the start of the dehydriding process (remained at a constant level afterwards) and a steady upward trend was observed for the β peak during the whole dehydriding process. This result demonstrates that microstrain (dislocation emission) might be built-up at β phase during the H_2 deloading stage. This indicates a completely different microstructural behavior compared to the H_2 absorption for the compact-structured Pd/Ti film which microstrain tended to build up at α phase (see 5.2.2). In addition, it was also interesting to discover that the microstrain was piled-up at β phase more rapidly as hydrogen loading and deloading cycle number increased. Combined with the results of the β-α phase transformed fraction as a function of time from D4 to D6 given in Figure 5.18, it seems that more defects including grain boundaries (acting as fast diffusion pathways to accelerate the β-α phase transition) and dislocations were probably generated simultaneously during H_2 desorption as H_2 loading/deloading cycle number increased. Further experimental or computational work is required to confirm the occurrence of this effect.

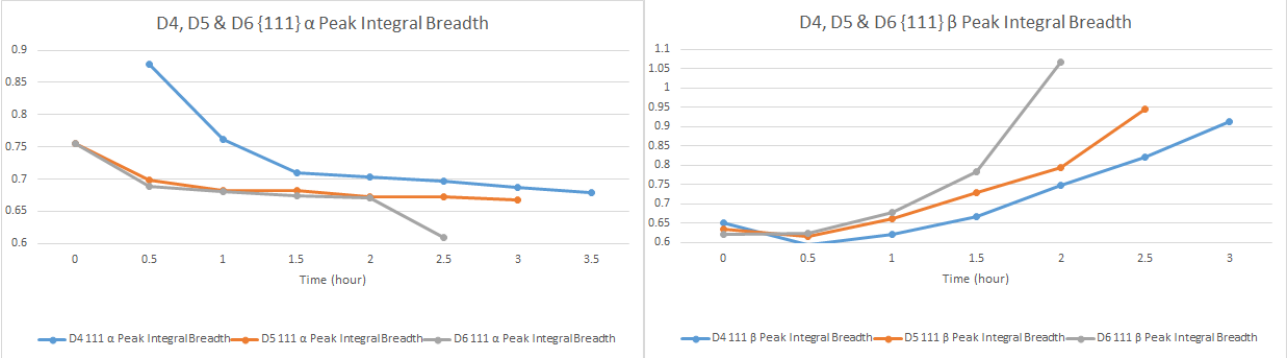

Figure 5.19: The changes of integral breadths of the {111} peak of the α phase (left figure) and β phase (right figure) during the H_2 absorption at D4, D5 and D6 for the compact-structured Pd/Ti sample.

5.3. Stress analysis for the open and compact-structured Pd/Ti thin films during H_2 absorption at different p(H_2) and desorption in N_2

Open-structured film: The calculated in-plane stress ($\sigma_{//}$) at each hydrogen loading and deloading cycles for the open-structured Pd/Ti are provided in Table 5.1. Compared with the stress history of the sample at L20 (p(H_2) = 0.05 atm) and D20 (the H_2 deloading cycle after L20) given in Figure 5.1 and 5.2, it could be noted that the compressive stress slightly increased at H_2 loading condition (p(H_2) = 0.05 atm) and the tensile stress remained at the same level at H_2 deloading condition during the 21st hydrogen loading/deloading cycle. Since the increase of compressive stress at H_2 loading condition is attributed to the lattice mismatch between the α and β phases (3.5 %) [18], the increase of the stress level at L21 confirms that the selected open-structured Pd/Ti thin film after experiencing 20 H_2 loading and deloading cycles behaved more similarly to the compact-structured Pd/Ti sample which accommodated less of the lattice expansion compared with the same sample at the original state. As a result, the α-β phase transition could only be 90% completed (shown in Figure 5.7) since the energy barrier of it was elevated by the larger compressive in-plane stress (see Equation 3.2). However, the stress level of L22 with a higher applied p(H_2) = 0.1 atm was found to be slightly lower than L21. This could be the results of the 100% complete α-β phase transition at L22 (see 5.2.1) which less stress was induced by the difference between the lattice constants of the α and β phases. Meanwhile, after applying the p(H_2) = 0.1 atm at L/D 22, the built-up compressive stress level decreases from 542 MPa to 478 MPa at L23 (p(H_2) = 0.05 atm). Connecting this result with the kinetic analysis of H_2 absorption at L23 (given in Figure 5.9), it seems that the Pd/Ti film behaved slightly similarly to the original open-structured Pd/Ti sample again accommodating more of the phase transition-induced lattice expansion compared to L21. Thus, the increasing stress could be slightly released which leaded to a higher transformed fraction and faster kinetics compared to L21. A possible explanation of this might be that extra spaces were created by the formation of microcracks to release the stress. Despite that the rearrangement of microcrack space was not observed at the Ti intermediate layer for the open structured Pd/Ti sample in the work done by Verma et al. probably due to the intrinsic low compliance of Ti [18], it could be argued that some cracks were initiated after the α-β phase transition fully completed at L22 (p(H_2) = 0.1 atm). Due to the limitation of the in-situ hydriding XRD analysis, the occurrence of the formation of microcrack network could not be confirmed, which is required to be further studied in the future work.

H_2 loading/deloading cycle number	H_2 loading ($\sigma_{//}$, MPa)	H_2 deloading ($\sigma_{//}$, MPa)
21 (p(H_2) = 0.05 atm)	(L21) -563 ±54	(D21) 570 ±6
22 (p(H_2) = 0.1 atm)	(L22) -542 ±26	(D22) 578 ±10
23 (p(H_2) = 0.05 atm)	(L23) -478 ±26	

Table 5.1: The stress states of L/D 21, L/D 22 and L23 for the open-structured Pd/Ti film.

Compact-structured film: For the compact-structured Pd/Ti, $\sigma_{//}$ at each H_2 loading and deloading cycle is given in Table 5.2. From L2 (p(H_2) = 0.05 atm) to L4 (p(H_2) = 0.1 atm), a downward trend of the compressive in-plane stress for the compact-structured Pd/Ti sample was identified. As same as the trend from L21 (p(H_2) = 0.05 atm) to L22 (p(H_2) = 0.1 atm) for the open-structured Pd/Ti sample, this could also probably be attributed to the 100% complete phase transition at higher p(H_2) at L4. However, it is clear that the stress level increased

significantly from L4 to L6 (not considering the data of L5 due to its large uncertainty) which behaved completely different from the open-structured Pd/Ti sample after loading at by higher p(H_2). This probably indicate that the compact-structured Pd/Ti became even "denser" after L4 at H_2 loading condition. Subsequently, the higher compressive level further restricted the absorption of hydrogen as depicted in Figure 5.11. By contrast, a decrease of the tensile stress level from D4 (550 MPa) to D5 (504 MPa) could be identified in Table 5.2, which might suggest that the tensile stress induced from the clamping effect during H_2 desorption could be slightly released from D4 to D5. This observation could explain the faster kinetics of β-α phase transition as the H_2 deloading cycle number increased (see Figure 5.18). The relaxation of tensile stress could probably be owing to higher dislocation density in the sample at D5 than at D4 as will be further explained in 5.4.

H_2 loading/deloading cycle number	H_2 loading ($\sigma_{//}$, MPa)	H_2 deloading ($\sigma_{//}$, MPa)
2 (p(H_2) = 0.05 atm)	(L2) -452 $\pm 0^a$	
4 (p(H_2) = 0.1 atm)	(L4) -425 ± 7	(D4) 550 ± 31
5 (p(H_2) = 0.05 atm)	(L5) -458 $\pm 169^b$	(D5) 504 ± 15
6 (p(H_2) = 0.05 atm)	(L6) -506 ± 30	

Table 5.2: The stress states of L2, L/D 4, L/D 5 and L6 for the compact-structured Pd/Ti film. a: The data of the long scan at $\psi = 60°$ for L2 could not to be collected. Thus, only two data points were extracted to calculate the stress and no uncertainty value could be obtained. b: The data of the short scans at $\psi = 26.57°$ and 33.21° at L5 was not available due to technical problems. Therefore, the data of long scans at $\psi = 20°$ and 40° for L5 was taken instead to calculate the stress which the results become less reliable since there is approximately 10° deviation from 29.5° (the wanted tilting angle as explained in 4.2.2 for both of the scans.)

5.4. Line-broadening analysis for open and compact-structured Pd/Ti thin films during H_2 absorption at different p(H_2) and desorption in N_2

In this section, the results of the calculated dislocation densities (ρ) and average crystallite from line-broadening analysis measured at $\psi = 0°$ to 60° for both of the open and compact-structured Pd/Ti samples at each measured H_2 loading and deloading cycle are going to be discussed. Since the exact same trend (from $\psi = 0°$ to 60°) could be attained by the line-broadening analysis with (L_f and sq_f, see 4.2.3) or without (h) correction from the instrumental profile, the trend instead of the exact value will be mainly concentrated at in this part. Only the results of sq_f will be provided in this section. The statistic error of 3 standard deviations (3 σ) is illustrated by the error bar for sq_f.

5.4.1. Line-broadening analysis for the open-structured Pd/Ti thin film during H_2 absorption at different p(H_2)

The comparison of the dislocation densities (ρ) at L21 (p(H_2) = 0.05 atm), L22 (p(H_2) = 0.1 atm) and L23 (p(H_2) = 0.05 atm) are shown in Figure 5.20. Comparing L21 and L22, it is clear that ρ was lower at higher applied p(H_2) (excluding $\psi = 60°$ which nearly the same ρ value was attained). The reason behind this result might be due to the 100% complete and quick α-β phase transition at L22 which limited the emission of dislocations in the α phase as discussed in 3.1. Moreover, it is interesting to see that after experiencing higher p(H_2) at L22, the dislocation density of L23 was found to be slightly lower than L21 at $\psi = 0°$ with the same applied p(H_2) = 0.05 atm. Combined with Figure 5.9 and Table 5.1, it was expected that the dislocation density at L23 should be higher than L21 since dislocation emission was assumed to be the main contributor of stress relaxation which apparently happened from L22 to L23 according to Table 5.1. However, since ρ was found to be lower at L23, it is probable that the pile-up compressive stress was released not solely by dislocation emission but also by the creation of microcracks, grain boundaries and/or voids which provided more space to accommodate the phase transition-induced volume expansion and accelerate the kinetics of hydrogen absorption [18]. Further experimental/computational studies are required to confirm this effect.

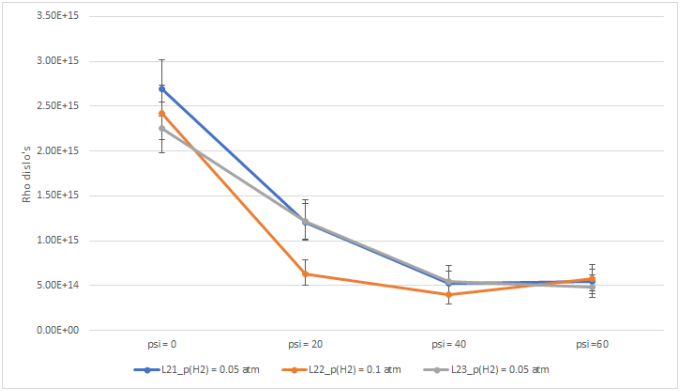

Figure 5.20: The comparison of the dislocation densities (ρ) at L21, L22 and L23 for the open-structured Pd/Ti sample with instrumental corrected profile (sq_f) as a function of tilt angle (ψ).

The trend of the average crystallite sizes during L21 ($p(H_2)$ = 0.05 atm), L22 ($p(H_2)$ = 0.1 atm) and L23 ($p(H_2)$ = 0.05 atm) is also given in Figure 5.21. It could be observed that the largest size was attained at ψ = 0° regardless of the cycle number. This could be attributed to the strong adhesive strength (clamping effect) provided by the Ti intermediate layer which restricted the lateral expansion and only allowed vertical expansion during the hydriding process (explained in section 2). Thus, the interplane distance between the crystallographic planes parallel to the surface were expected to be significantly larger than the interplane distance of other planes. Combined with the results of ρ at L21, L22 and L23 given in Figure 5.20, it could also be concluded that the restriction of lateral expansion leaded to a higher dislocation density found at ψ = 0° (crystallographic plane parallel to the surface) than other tilting angles since the grains tended to expand at the out-of-plane direction rather than in-plane direction. Unfortunately, since the crystallite size differences between L21, L22 and L23 were all within the error bar (see the middle of Figure 5.21), the evolution of the crystallite size during the loading cycles for the sample could not be concluded.

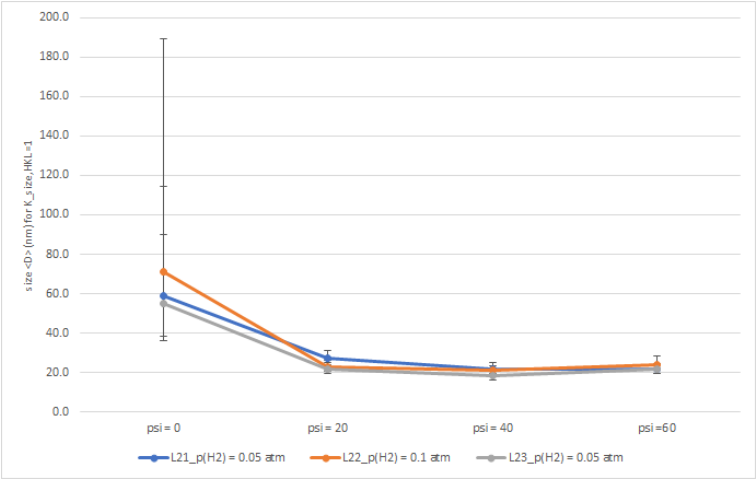

Figure 5.21: The comparison of the average crystallite sizes (D) at L21, L22 L23 for the open-structured Pd/Ti sample with instrumental corrected profile (sq_f) as a function of tilt angle (ψ).

5.4.2. Line-broadening analysis for the compact-structured Pd/Ti thin film during H_2 absorption at different $p(H_2)$

The results of the comparison between ρ of L4 ($p(H_2)$ = 0.1 atm), L5 ($p(H_2)$ = 0.05 atm) and L6 ($p(H_2)$ = 0.05 atm) are shown in Figure 5.22. Compared with the results of the open-structured Pd/Ti sample during H_2 loadeing cycles (see Figure 5.20), it is clear that the microstructural behavior of the compact-structured Pd/Ti thin film after applying the $p(H_2)$ = 0.1 atm is apparently different from the open-structured one. First of all, the order of ρ from high to low at ψ = 0° and 20° (L4 > L5 > L6) is the opposite of the order of ρ at 40° and 60° (L6 > L5 > L4), which is completely different from the open-structured one (see Figure 5.20). This could be

attributed to the texture difference between the two samples illustrated by the Pd{111} fiber texture plot (FTP) (see Figure 5.24 done by Verma et al., which shows that the compact-structured Pd/Ti was textured much more strongly than the open-structured one owing to the different deposition pressure as explained in 4.1. Hence, the microstructural behavior including dislocation emission were expected to be different at different planes (ψ angles) for the compact-structured Pd/Ti thin film which matched the results given in Figure 5.22. By contrast, the behavior of dislocation emission should be similar among all the different planes for the open-structured Pd/Ti film with a much broader texture (see Figure 5.20).

Meanwhile, it is important to notice that ρ at L4 ($p(H_2)$ = 0.1 atm) was significantly higher than L5 and L6 ($p(H_2)$ = 0.05 atm) and slightly higher than L2 ($p(H_2)$ = 0.05 atm) (referred to Figure 5.23) at $\psi = 0°$. Combined these results with Table 5.2 which shows that the lowest compressive stress was found at L4 among all the H_2 loading cycles, it seems that more stress could be released by dislocation emission when higher $p(H_2)$ was applied to complete the α-β phase transition with sufficient amount of transition time (around 1 to 2 hours as depicted in Figure 5.14) unlike L22 which the "quasi-equilibrium" point was reached in less than 3 minutes (explained in 5.2.1). The reason why more dislocations could be generated at L4 than L5 and L6 at $\psi = 0°$ might be provided in Figure 5.25 which shows that the average crystallite size of L4 at $\psi = 0°$ (47.8 nm for sq_f) was larger than L5 (38.6 nm for sq_f) and L6 (37.0 nm for sq_f) despite that the error bar overlapped with each cycle. As a result, the critical thickness of Pd hydride thin film (reported to be 22 nm to 34 nm [48]) to release the stress by the emission of dislocations at the α-β phase interfaces could be reached for L4 at $\psi = 0°$ [21]. On the other hand, the dislocation emission at the phase interfaces might be suppressed at L5 and L6 since the critical thickness was not reached, thus, larger value of compressive stress were expected [21] which matches the results of stress measurements revealed in Table 5.2.

In addition, the reverse order of ρ from high to low at $\psi = 40°$ and 60° compared to the order at $\psi = 0°$ and 20° could also be attributed to the different crystallographic planes for dislocation initiation after the larger plastic deformation induced by larger number of dislocation emissions during L4 at higher $p(H_2)$ for the compact-structured Pd/Ti thin film. Further studies are probably required to interpret this result since it is not within the scope of this research.

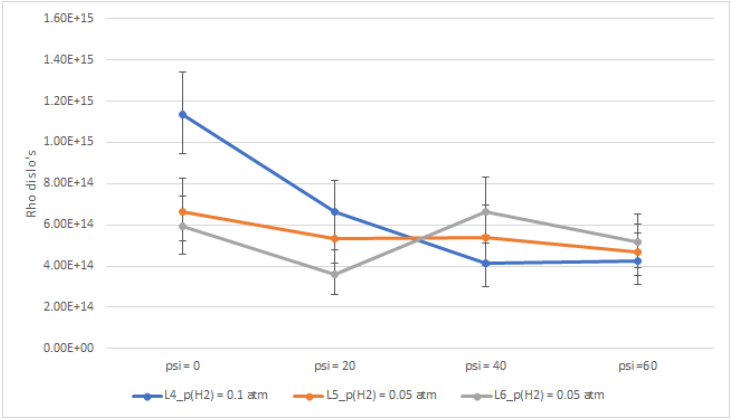

Figure 5.22: The comparison of the dislocation densities (ρ) at L4, L5 L6 for the compact-structured Pd/Ti sample with instrumental corrected profile (sq_f) as a function of tilt angle (ψ).

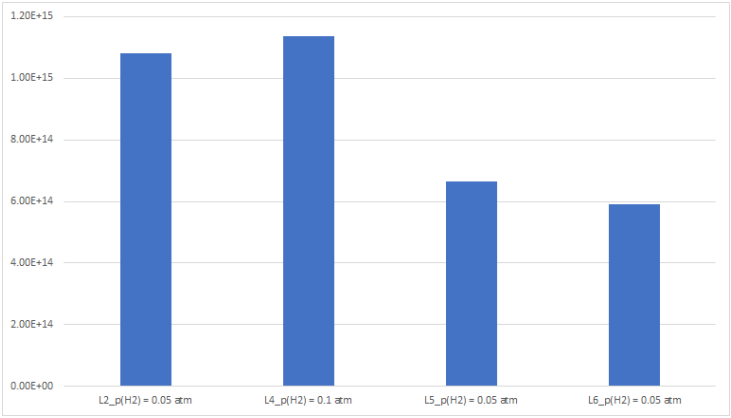

Figure 5.23: The comparison of the dislocation densities (ρ) at L2, L4, L5 and L6 at $\psi = 0°$ for the compact-structured Pd/Ti sample with instrumental corrected profile (sq_f).

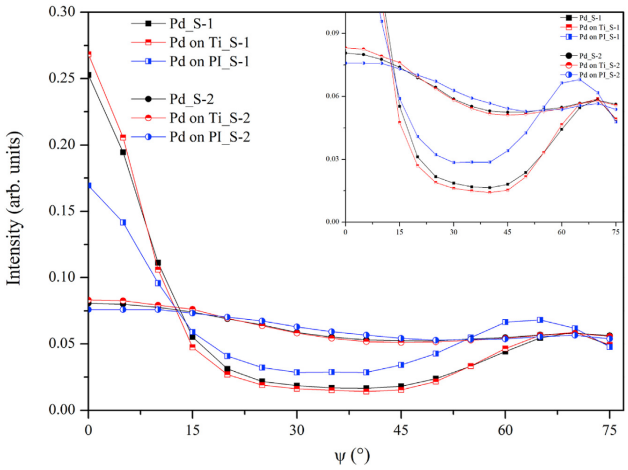

Figure 5.24: The Pd{111} fiber texture plot (FTP) of the compact-structured (represented by Pd on Ti_S-1) and open-structured (represented by Pd on Ti_S-2) Pd/Ti sample as a function of tilt angle (ψ). Ref: [18]

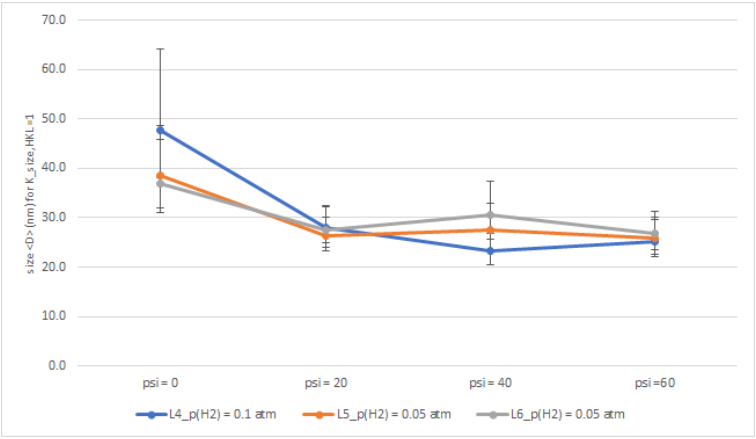

Figure 5.25: The comparison of the average crystallite sizes (D) at L4, L5 L6 for the compact-structured Pd/Ti sample with instrumental corrected profile (sq_f) as a function of tilt angle (ψ).

5.4.3. Line-broadening analysis for the open-structured Pd/Ti thin film during H_2 desorption in N_2

Figure 5.26 shows the change of ρ from D21 (after L21 loading at p(H_2) = 0.05 atm) to D22 (after L22 loading at p(H_2) = 0.1 atm). From the figure, ρ was found to be higher at D22 especially at $\psi = 0°$ and 40° which the differences were larger than the error bar for sq_f. Since the data of the kinetic analysis for D21 could not be collected (explained in Figure 5.16), the correlation between the H_2 desorbing properties and dislocation densities could not be defined. Nevertheless, this result might still be an indicator that more dislocation were generated during H_2 desorption to trigger microstructural changes (as suggested in 5.2.1 and 5.2.3 after H_2 loading cycle number 22 which the α-β phase transition was rapidly and fully completed. In terms of the average crystallite size at D21 and D22 as depicted in Figure 5.27, a similar trend as at L21 and L22 was identified with a slightly larger value, which is hard to be interpreted as well.

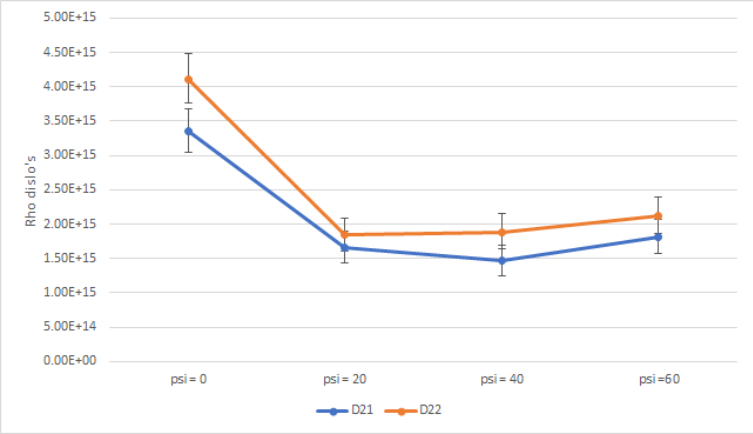

Figure 5.26: The comparison of the dislocation densities (ρ) at D21 and D22 for the open-structured Pd/Ti sample with instrumental corrected profile (sq_f) as a function of tilt angle (ψ).

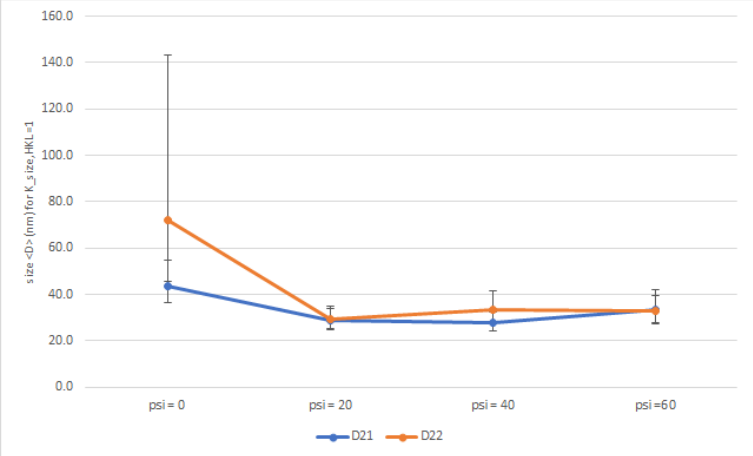

Figure 5.27: The comparison of the average crystallite sizes (D) at D21 and D22 for the open-structured Pd/Ti sample with instrumental corrected profile (sq_f) as a function of tilt angle (ψ).

5.4.4. Line-broadening analysis for the compact-structured Pd/Ti thin film during H_2 desorption in N_2

From D4 (after L4 loading at p(H_2) = 0.1 atm) to D5 (after L5 loading at p(H_2) = 0.05 atm), the changes of dislocation densities and crystallite sizes are shown in Figure 5.28 and 5.29, respectively. In terms of ρ, it could be seen that the trend of D4 was completely same as L4 (see Figure 5.22). However, ρ was found to be significantly higher for D5 than D4 at $\psi = 20°$ and 40°, which is a different trend compared with Figure 5.22

depicting ρ of L4 and L5. Meanwhile, the average crystallite size of D5 at $\psi = 20°$ (40.1 nm for sq_f) and 40° (36.4 nm for sq_f) was also found to be higher than D4 at $\psi = 20°$ (30.4 nm for sq_f) and 40° (25.0 nm for sq_f). Combined these results with Table 5.2, it could be suggested that the internal tensile stress induced by the clamping effect during H_2 desorption at D5 could probably be partially released by dislocation emitted at the crystallographic planes non-parallel to the film surface where the critical thickness of the film for dislocation emission was reached (as explained in 5.4.2). Subsequently, the kinetics of H_2 desorption was faster than D4 as illustrated in Figure 5.18. However, the exact mechanism behind this phenomenon could not be explained within the framework of this work, thus, further work is required to further understand this effect.

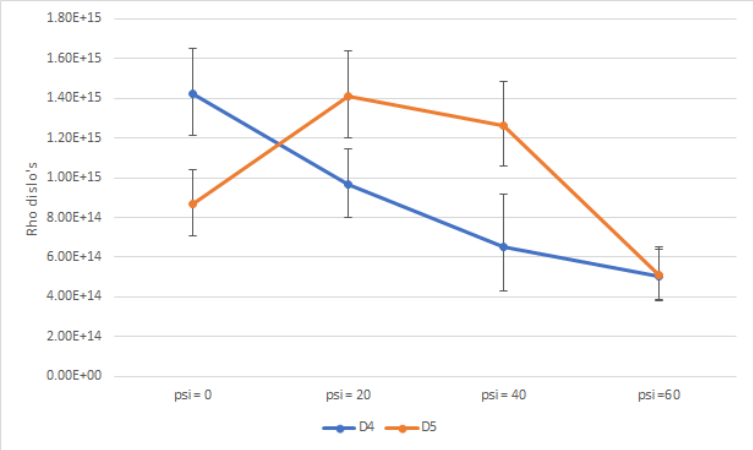

Figure 5.28: The comparison of the dislocation densities (ρ) at D4 and D5 for the compact-structured Pd/Ti sample with instrumental corrected profile (sq_f) as a function of tilt angle (ψ).

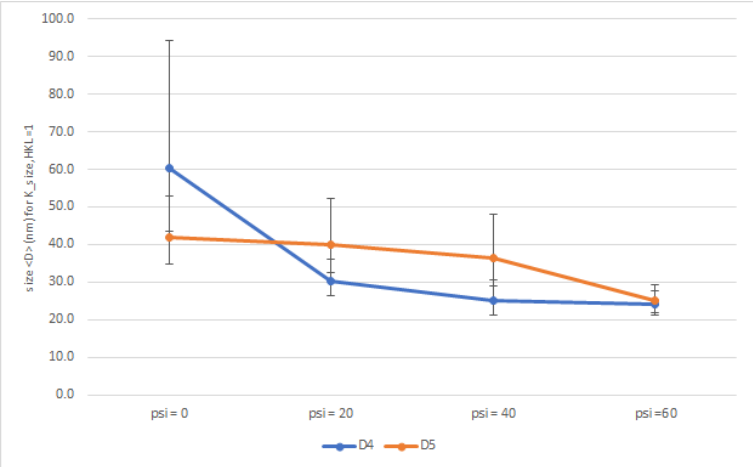

Figure 5.29: The comparison of the average crystallite sizes (D) at D4, D5 for the compact-structured Pd/Ti sample with instrumental corrected profile (sq_f) as a function of tilt angle (ψ).

6. Conclusion

In this research, in-situ hydriding X-ray Diffraction study adopting macrostress and XRD line-broadening analysis was applied to analyze the kinetics, stress states and microstrucural evolution (dislocation emission) of both of the open and compact-structured Pd/Ti thin films during H_2 absorption and desorption to further understand the influence of different morphologies on H_2 absorbing and desorbing properties. Higher p(H_2) (0.1 atm) compared with the work done by Verma et al. (lower p(H_2) = 0.05 atm, [18]) was applied in order to fully overcome the energy barrier of α-β phase transition for both of the samples and observe the corresponding kinetic/stress/microstructural changes.

H_2 absorption for open-structured Pd/Ti thin film: After 20 H_2 loading and deloading cycles, the α-β phase transition was only 90% completed in 1 hour at the next H_2 loading cycle (L21) at lower p(H_2), and the microstrain was found to build up in α phase. To overcome the energy barrier of the α-β phase transition, higher p(H_2) was applied at the next cycle (L22). As a result, the α-β phase transition could be 100% completed in less than 3 minutes, which means that the sloped-energy barrier of the transition could be fully overcome by the higher applied p(H_2). Dislocation emissions were suppressed at this cycle since the "quasi-equilibrium" time for the α-β phase transition is probably too short for dislocation generation. Thus, stress relaxation was not obvious at this cycle. On the other hand, stress relaxation seemed to occur at the next H_2 loading cycle (L23) loading at lower p(H_2) again. Compared with L21, higher phase transformed fraction and shorter "quasi-equilibrium" phase transition time were observed at L23, and there is no indicator of the location of microstrain initiation during this H_2 loading cycle. These observations suggest that the microstructural changes such as crack initiations occurred after applying higher p(H_2) by hydrogen gas thereby creating more space for accommodating the α-β phase transition-induced volume expansion. Further experimental/computational work is required to establish this result.

H_2 desorption for open-structured Pd/Ti thin film: It was observed that the kinetics of the β-α phase transition at D23 (after loading at lower p(H_2)) is slower than D22 (after loading at higher p(H_2)). This might be attributed to the higher number of remaining dislocations at L23 than L22 acting as unoccupied trapping sites for H atoms to slow down the kinetics.

H_2 absorption for compact-structured Pd/Ti thin film: After 1 H_2 loading and deloading cycle was completed, the α-β phase transition was 92% completed in 5 hours at the next H_2 loading cycle (L2) at lower p(H_2). Compared with the open-structured Pd/Ti loading at the same p(H_2), similar level of phase transformed fraction was observed with a slower kinetics. To overcome the energy barrier of the α-β phase transition, higher p(H_2) was applied at the 4th H_2 loading cycle. Then, the α-β phase transition could be 100% completed in less than 2 hours, which means that the sloped-energy barrier of the transition could also be fully overcome by the higher applied p(H_2). Stress relaxation by dislocation emissions occurred at this cycle since the average crystallite size was significantly larger than the critical thickness of the Pd thin film for dislocation generation. On the other hand, stress relaxation by introducing dislocations was suppressed at the next two cycles (L5 and L6) loading at lower p(H_2) probably owing to the insufficient Pd thickness to introduce dislocations. Hence, the phase transformed fraction become much lower (L5: 77%; L6: 81%) with a much longer "quasi-equilibrium" time (30 hours for L5 and L6) compared with L2. For all the H_2 loading cycles, it was found that microstrain was built-up at α phase, which is similar to L21 for the open-structured Pd/Ti. However, the emission of dislocations tended to occur at the crystallographic planes non-parallel to the film surface especially after higher p(H_2) was applied, which is a completely different behavior compared with the open-structured Pd/Ti. This might be due to the textural differences between the open and compact-structured Pd/Ti thin films or some other underlying causes for the different locations for dislocation initiations which could not be addressed within the scope of this work.

H_2 desorption for compact-structured Pd/Ti thin film: The kinetics of the β-α phase transition at D5 (after loading at lower p(H_2)) and D6 (after loading at lower p(H_2)) were found to be faster than D4 (after loading at higher p(H_2)). This might be due to the occurrence of stress relaxation since the average crystallite size (at $\psi = 20^\circ$ and 40°) at D5 was larger than the critical Pd thickness to introduce dislocations at the planes non-parallel to the surface. However, the exact mechanism behind this phenomenon could not be explained within the framework of this work. During the phase transition, microstrain was built up at β phase. This is a different microstructural behavior from H_2 absorption which microstrain tends to build up at α phase. Furthermore, more microstrain was built up as cycle number increases. This probably indicates that more defects were generated. Both of the results also require further studies to be established.

7. Recommendation

The following recommendations are listed for further research:

- The fitting for the Si substrate-induced reflections could probably be fitted more accurately by adopting a non-linear polynomial background instead of using solely Gaussian function with linear background signal.
- Within the scope of this research, the pure screw dislocation with randomly oriented 111, a/2<110> slip system was assumed to be the only type of emitted dislocations. However, due to the intrinsic anisotropic characteristics of the Pd/Ti thin films, the dislocations might be orientation dependent. Also, a certain fraction of the emitted dislocations might actually be edge dislocations with different slip systems. Thus, a model considering both screw and edge dislocations with directional preference could be developed to improve the line-broadening analysis of the Pd/Ti thin films.
- In this research, a simplified model of an isotropic system using biaxial state of stress was used to estimate the in-plane stress. More advanced model for stress determination in a thin film could be used to take into account of texture and grain orientation to cope with the intrinsic anisotropic properties of the Pd/Ti thin film.
- The role of crack initiation (or growth) as a mechanism to release stress should be further investigated.
- In this work, the average crystallite size (D) was estimated purely from line-broadening analysis. Despite the calculated size seems to be reasonable and interpretable, D was found to be sensitive to the fitting (especially at $\psi = 0^\circ$ with Gaussian function-corrected instrumental profile where the error bar was extremely large for both of the Pd/Ti samples). Thus, the development of the in-situ measurements to determine the average crystallite size of the Pd/Ti thin film with higher accuracy during H_2 absorption and desorption is prbably required to attain better estimation of the size of the Pd crystallites.

References

[1] B. D. Adams and A. Chen, "The role of palladium in a hydrogen economy," *Materials today*, vol. 14, no. 6, pp. 282–289, 2011.

[2] J. O. Abe, A. Popoola, E. Ajenifuja, and O. Popoola, "Hydrogen energy, economy and storage: review and recommendation," *International Journal of Hydrogen Energy*, vol. 44, no. 29, pp. 15 072–15 086, 2019.

[3] F. Manchester, A. San-Martin, and J. Pitre, "The H-Pd (hydrogen-palladium) system," *Journal of phase equilibria*, vol. 15, no. 1, pp. 62–83, 1994.

[4] R. K. Joshi, S. Krishnan, M. Yoshimura, and A. Kumar, "Pd nanoparticles and thin films for room temperature hydrogen sensor," *Nanoscale research letters*, vol. 4, no. 10, pp. 1191–1196, 2009.

[5] J. Dai, L. Zhu, G. Wang, F. Xiang, Y. Qin, M. Wang, and M. Yang, "Optical fiber grating hydrogen sensors: A review," *Sensors*, vol. 17, no. 3, p. 577, 2017.

[6] M. Yamauchi, H. Kobayashi, and H. Kitagawa, "Hydrogen storage mediated by Pd and Pt nanoparticles," *ChemPhysChem*, vol. 10, no. 15, pp. 2566–2576, 2009.

[7] G. Li, H. Kobayashi, J. M. Taylor, R. Ikeda, Y. Kubota, K. Kato, M. Takata, T. Yamamoto, S. Toh, S. Matsumura *et al.*, "Hydrogen storage in Pd nanocrystals covered with a metal–organic framework," *Nature materials*, vol. 13, no. 8, pp. 802–806, 2014.

[8] G. Grashoff, C. Pilkington, and C. Corti, "The purification of hydrogen," *Platinum Metals Review*, vol. 27, no. 4, pp. 157–169, 1983.

[9] E. Antolini, "Palladium in fuel cell catalysis," *Energy & Environmental Science*, vol. 2, no. 9, pp. 915–931, 2009.

[10] J. Okazaki, T. Ikeda, D. A. P. Tanaka, K. Sato, T. M. Suzuki, and F. Mizukami, "An investigation of thermal stability of thin palladium–silver alloy membranes for high temperature hydrogen separation," *Journal of Membrane Science*, vol. 366, no. 1-2, pp. 212–219, 2011.

[11] N. Al-Mufachi, N. Rees, and R. Steinberger-Wilkens, "Hydrogen selective membranes: A review of palladium-based dense metal membranes," *Renewable and Sustainable Energy Reviews*, vol. 47, pp. 540–551, 2015.

[12] M. Rahimpour, F. Samimi, A. Babapoor, T. Tohidian, and S. Mohebi, "Palladium membranes applications in reaction systems for hydrogen separation and purification: A review," *Chemical Engineering and Processing: Process Intensification*, vol. 121, pp. 24–49, 2017.

[13] A. Pundt and R. Kirchheim, "Hydrogen in metals: microstructural aspects," *Annu. Rev. Mater. Res.*, vol. 36, pp. 555–608, 2006.

[14] R. Kirchheim, T. Mütschele, W. Kieninger, H. Gleiter, R. Birringer, and T. Koble, "Hydrogen in amorphous and nanocrystalline metals," *Materials science and engineering*, vol. 99, no. 1-2, pp. 457–462, 1988.

[15] H. Iwaoka, M. Arita, and Z. Horita, "Hydrogen diffusion in ultrafine-grained palladium: Roles of dislocations and grain boundaries," *Acta Materialia*, vol. 107, pp. 168–177, 2016.

[16] T. C. Narayan, F. Hayee, A. Baldi, A. L. Koh, R. Sinclair, and J. A. Dionne, "Direct visualization of hydrogen absorption dynamics in individual palladium nanoparticles," *Nature communications*, vol. 8, no. 1, pp. 1–8, 2017.

[17] A. Ulvestad and A. Yau, "The self-healing of defects induced by the hydriding phase transformation in palladium nanoparticles," *Nature communications*, vol. 8, no. 1, pp. 1–6, 2017.

[18] N. Verma, R. Delhez, N. M. van der Pers, F. D. Tichelaar, and A. J. Böttger, "The role of the substrate on the mechanical and thermal stability of Pd thin films during hydrogen (de) sorption," *international journal of hydrogen energy*, vol. 46, no. 5, pp. 4137–4153, 2021.

[19] B. Amin-Ahmadi, D. Connétable, M. Fivel, D. Tanguy, R. Delmelle, S. Turner, L. Malet, S. Godet, T. Pardoen, J. Proost *et al.*, "Dislocation/hydrogen interaction mechanisms in hydrided nanocrystalline palladium films," *Acta Materialia*, vol. 111, pp. 253–261, 2016.

[20] R. Gremaud, M. Gonzalez-Silveira, Y. Pivak, S. De Man, M. Slaman, H. Schreuders, B. Dam, and R. Griessen, "Hydrogenography of PdHx thin films: Influence of H-induced stress relaxation processes," *Acta Materialia*, vol. 57, no. 4, pp. 1209–1219, 2009.

[21] S. Wagner and A. Pundt, "Quasi-thermodynamic model on hydride formation in palladium–hydrogen thin films: Impact of elastic and microstructural constraints," *International Journal of Hydrogen Energy*, vol. 41, no. 4, pp. 2727–2738, 2016.

[22] N. Verma, G. Krishnamurthy, F. D. Tichelaar, and A. J. Böttger, "Controlling morphology and texture of sputter-deposited Pd films by tuning the surface topography of the (Ti) adhesive layer," *Surface and Coatings Technology*, vol. 359, pp. 24–34, 2019.

[23] J. Čížek, O. Melikhova, M. Vlček, F. Lukáč, M. Vlach, I. Procházka, W. Anwand, G. Brauer, A. Mücklich, S. Wagner *et al.*, "Hydrogen-induced microstructural changes of Pd films," *international journal of hydrogen energy*, vol. 38, no. 27, pp. 12 115–12 125, 2013.

[24] C. San Marchi and B. P. Somerday, "Thermodynamics of gaseous hydrogen and hydrogen transport in metals," *MRS Online Proceedings Library (OPL)*, vol. 1098, 2008.

[25] D. Papaconstantopoulos, B. Klein, E. Economou, and L. Boyer, "Band structure and superconductivity of PdDx and PdHx," *Physical Review B*, vol. 17, no. 1, p. 141, 1978.

[26] H. Wagner and H. Horner, "Elastic interaction and the phase transition in coherent metal-hydrogen systems," *Advances in Physics*, vol. 23, no. 4, pp. 587–637, 1974.

[27] I. Petrov, P. Barna, L. Hultman, and J. Greene, "Microstructural evolution during film growth," *Journal of Vacuum Science & Technology A: Vacuum, Surfaces, and Films*, vol. 21, no. 5, pp. S117–S128, 2003.

[28] J. A. Thornton, "Influence of apparatus geometry and deposition conditions on the structure and topography of thick sputtered coatings," *Journal of Vacuum Science and Technology*, vol. 11, no. 4, pp. 666–670, 1974.

[29] U. Welzel, J. Ligot, P. Lamparter, A. Vermeulen, and E. J. Mittemeijer, "Stress analysis of polycrystalline thin films and surface regions by X-ray diffraction," *Journal of Applied Crystallography*, vol. 38, no. 1, pp. 1–29, 2005.

[30] U. Welzel and E. J. Mittemeijer, "Diffraction stress analysis of macroscopically elastically anisotropic specimens: On the concepts of diffraction elastic constants and stress factors," *Journal of Applied Physics*, vol. 93, no. 11, pp. 9001–9011, 2003.

[31] U. Welzel and E. Mittemeijer, "Applicability of the crystallite group method to fibre textured specimens," *Materials Science Forum*, vol. 443, pp. 131–136, 2004.

[32] B. D. Cullity, *Elements of X-ray Diffraction*. Addison-Wesley Publishing, 1956.

[33] D. Hsu and R. Leisure, "Elastic constants of palladium and β-phase palladium hydride between 4 and 300 K," *Physical Review B*, vol. 20, no. 4, p. 1339, 1979.

[34] P. Scardi, M. Leoni, and R. Delhez, "Line broadening analysis using integral breadth methods: a critical review," *Journal of Applied Crystallography*, vol. 37, no. 3, pp. 381–390, 2004.

[35] WaveMetrics, "Igor pro (8.03)," 2019. [Online]. Available: https://www.wavemetrics.com/

[36] T. H. De Keijser, J. Langford, E. J. Mittemeijer, and A. Vogels, "Use of the Voigt function in a single-line method for the analysis of X-ray diffraction line broadening," *Journal of Applied Crystallography*, vol. 15, no. 3, pp. 308–314, 1982.

[37] R. Delhez, T. H. De Keijser, and E. Mittemeijer, "Determination of crystallite size and lattice distortions through X-ray diffraction line profile analysis," *Fresenius' Zeitschrift für analytische Chemie*, vol. 312, no. 1, pp. 1–16, 1982.

[38] P. Healey and J. Ayers, "The instrumental broadening function of the Bartels five-crystal X-ray diffractometer," *Acta Crystallographica Section A: Foundations of Crystallography*, vol. 52, no. 2, pp. 245–250, 1996.

[39] R. W. Cheary, A. A. Coelho, and J. P. Cline, "Fundamental parameters line profile fitting in laboratory diffractometers," *Journal of Research of the National Institute of Standards and Technology*, vol. 109, no. 1, p. 1, 2004.

[40] Bruker AXS GmbH, "DIFFRAC plus TOPAS (4.2)," 2009. [Online]. Available: https://www.bruker.com/en/products-and-solutions/diffractometers-and-scattering-systems/x-ray-diffractometers/diffrac-suite-software/diffrac-topas.html

[41] T. Ungár and A. Borbély, "The effect of dislocation contrast on x-ray line broadening: a new approach to line profile analysis," *Applied Physics Letters*, vol. 69, no. 21, pp. 3173–3175, 1996.

[42] T. Ungár, M. Leoni, and P. Scardi, "The dislocation model of strain anisotropy in whole powder-pattern fitting: the case of an Li–Mn cubic spinel," *Journal of applied crystallography*, vol. 32, no. 2, pp. 290–295, 1999.

[43] I. Groma, T. Ungár, and M. Wilkens, "Asymmetric X-ray line broadening of plastically deformed crystals. I. Theory," *Journal of applied crystallography*, vol. 21, no. 1, pp. 47–54, 1988.

[44] T. Ungár, I. Dragomir, Á. Révész, and A. Borbély, "The contrast factors of dislocations in cubic crystals: the dislocation model of strain anisotropy in practice," *Journal of applied crystallography*, vol. 32, no. 5, pp. 992–1002, 1999.

[45] N. van der Pers, "Experiment with a number of loading/deloading (l/d) cycles on the psi system for specimen pdti 300117-15min," unpublished.

[46] H. Jeong, M. Jin, K. So, S. Lim, and Y. Lee, "Tailoring the characteristics of graphite oxides by different oxidation times," *Journal of Physics D: Applied Physics*, vol. 42, no. 6, p. 065418, 2009.

[47] M. Etheridge and J. Wilkie, "Grainsize reduction, grain boundary sliding and the flow strength of mylonites," *Tectonophysics*, vol. 58, no. 1-2, pp. 159–178, 1979.

[48] S. Wagner, H. Uchida, V. Burlaka, M. Vlach, M. Vlcek, F. Lukac, J. Cizek, C. Baehtz, A. Bell, and A. Pundt, "Achieving coherent phase transition in palladium–hydrogen thin films," *Scripta Materialia*, vol. 64, no. 10, pp. 978–981, 2011.

8. Appendix

8.1. Diffraction patterns of L20 ($p(H_2) = 0.05$ atm) and D20 for the open-structured Pd/Ti film

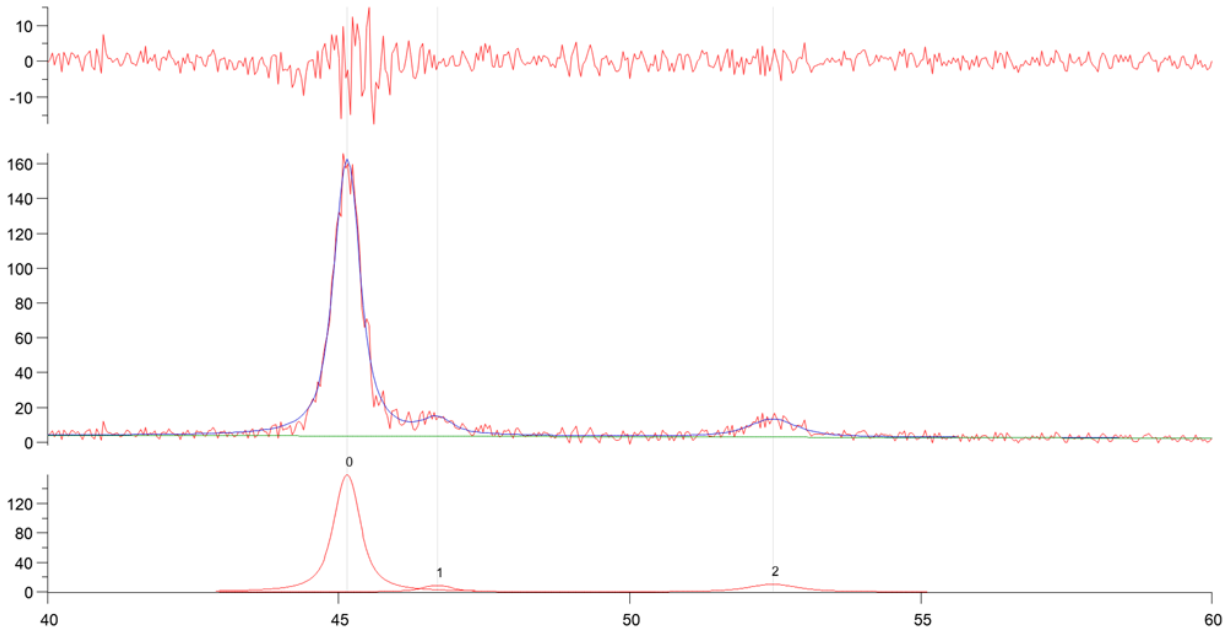

Figure 8.1: The diffraction pattern of {111} and {200} peaks at L20 ($p(H_2) = 0.05$ atm).

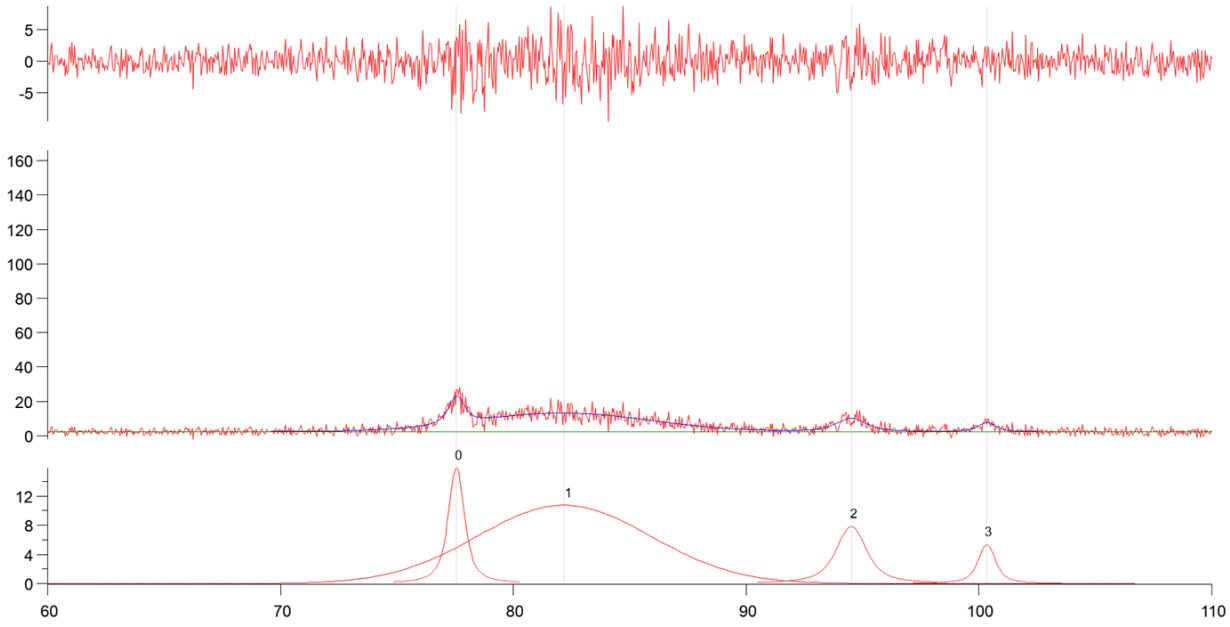

Figure 8.2: The diffraction pattern of {220} + Si/SiO_2-induced reflections + {311} + {222} peaks at L20 ($p(H_2)$ = 0.05 atm).

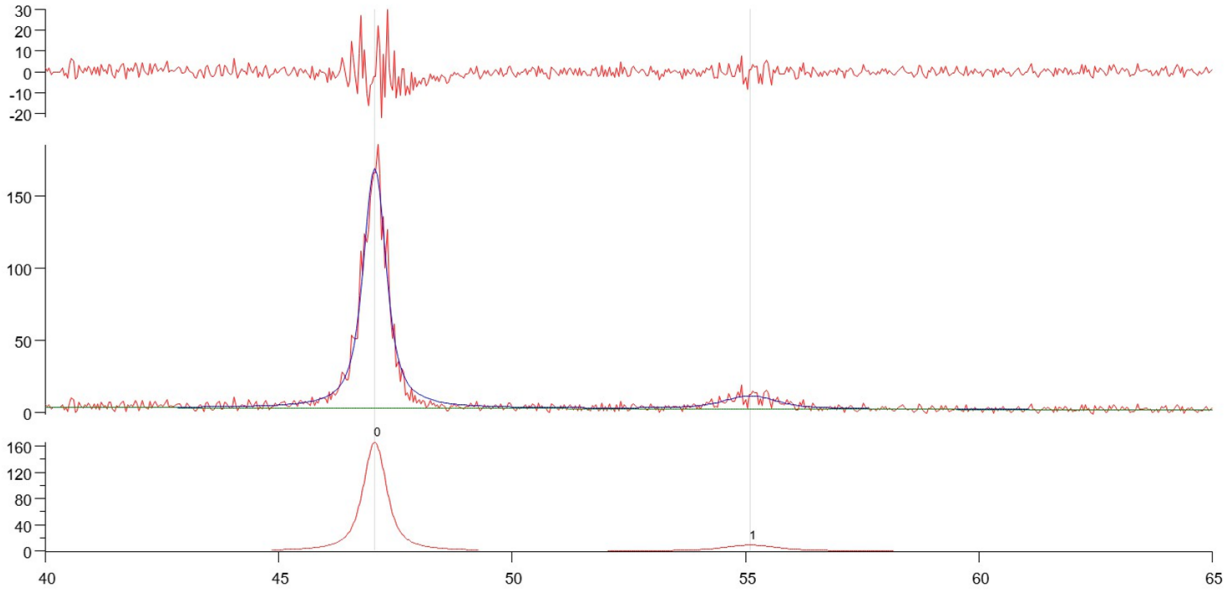

Figure 8.3: The diffraction pattern of {111} and {200} peaks at D20 (after loading at p(H_2) of 0.05 atm).

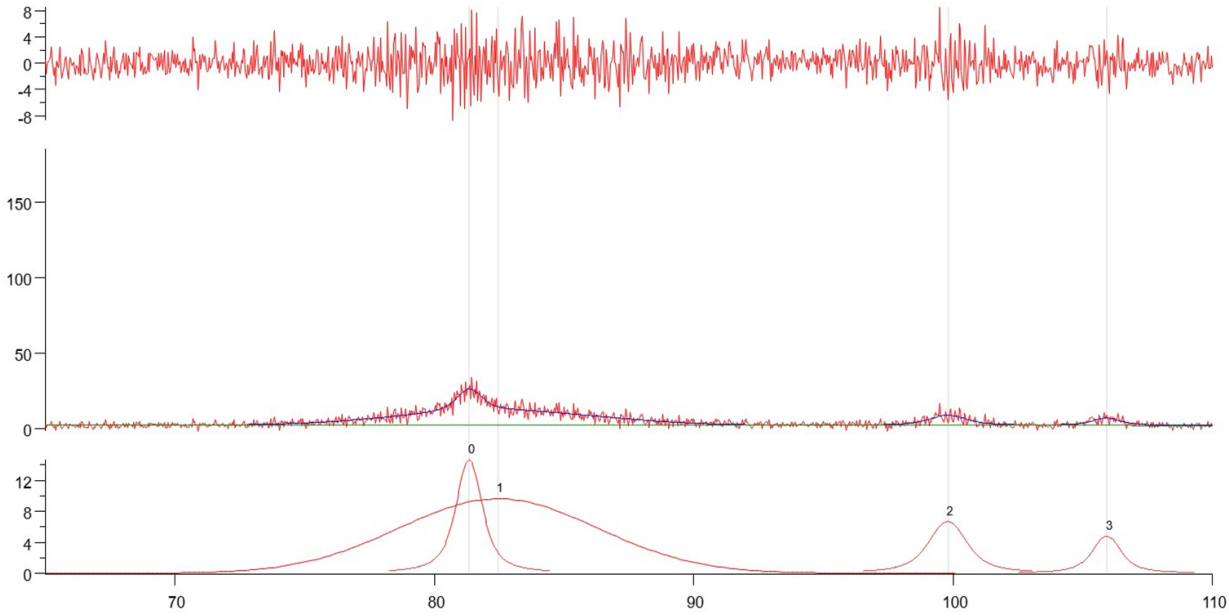

Figure 8.4: The diffraction pattern of {220} + Si/SiO_2-induced reflections + {311} + {222} peaks at D20 (after loading at p(H_2) of 0.05 atm).

8.2. Diffraction patterns (long scans) of L21 ($p(H_2) = 0.05$ atm), L22 ($p(H_2) = 0.1$ atm), and L23 ($p(H_2) = 0.05$ atm) for the open-structured Pd/Ti film

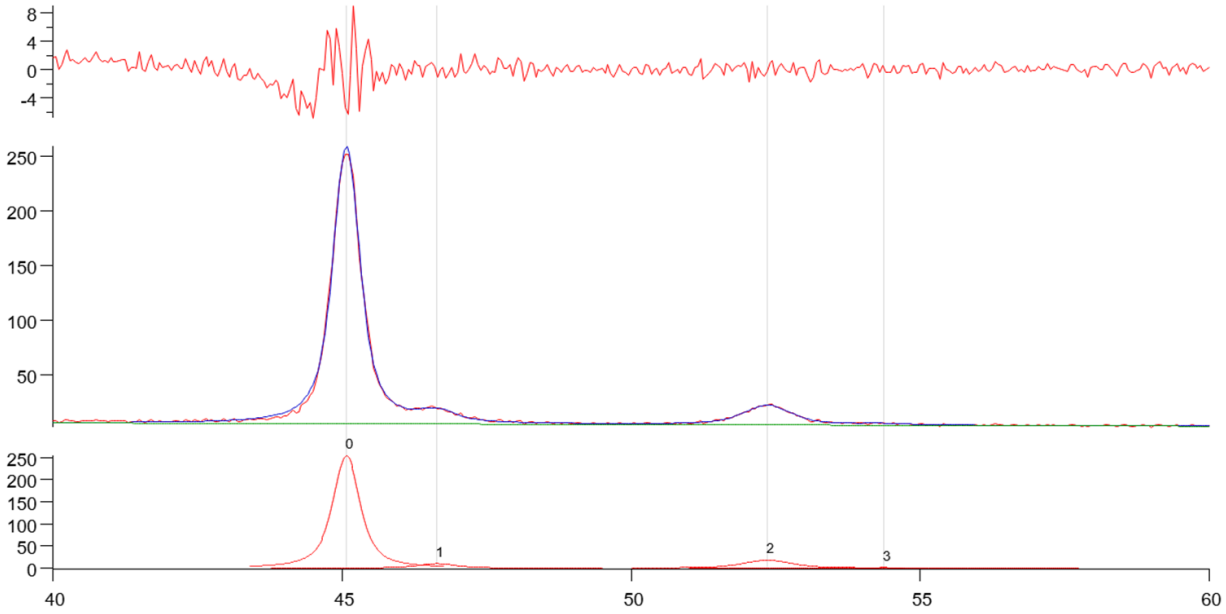

Figure 8.5: The diffraction pattern of {111} + {200} peaks at L21 ($p(H_2) = 0.05$ atm) at $\psi = 0°$.

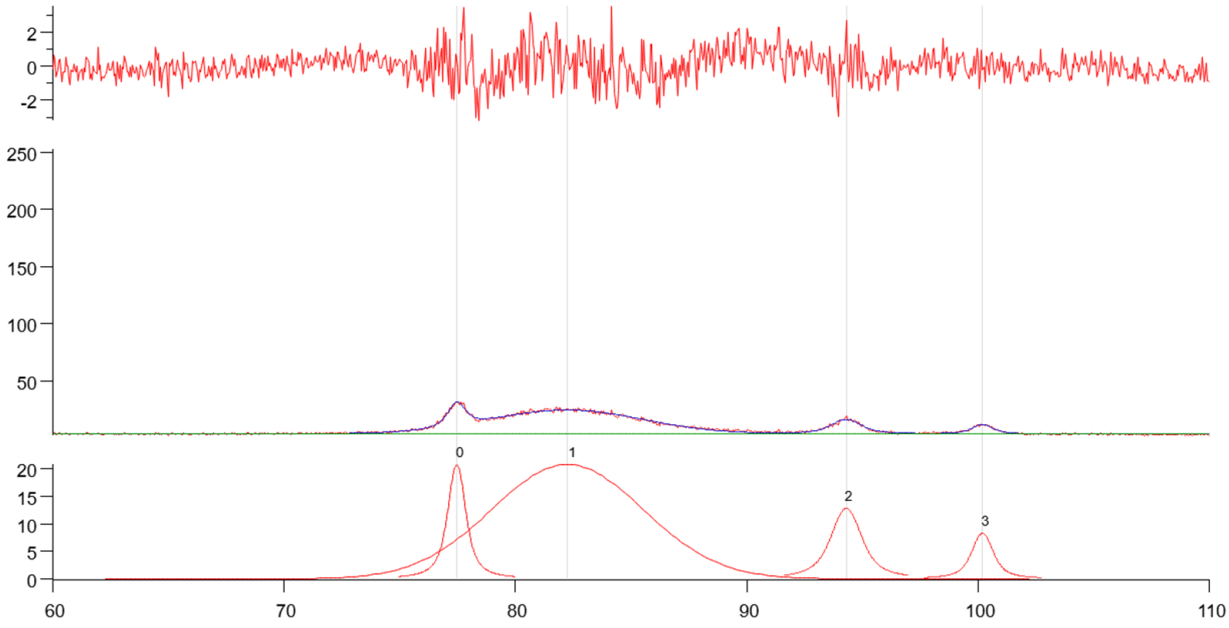

Figure 8.6: The diffraction pattern of {220} + Si/SiO_2-induced reflections + {311} + {222} peaks at L21 ($p(H_2) = 0.05$ atm) at $\psi = 0°$.

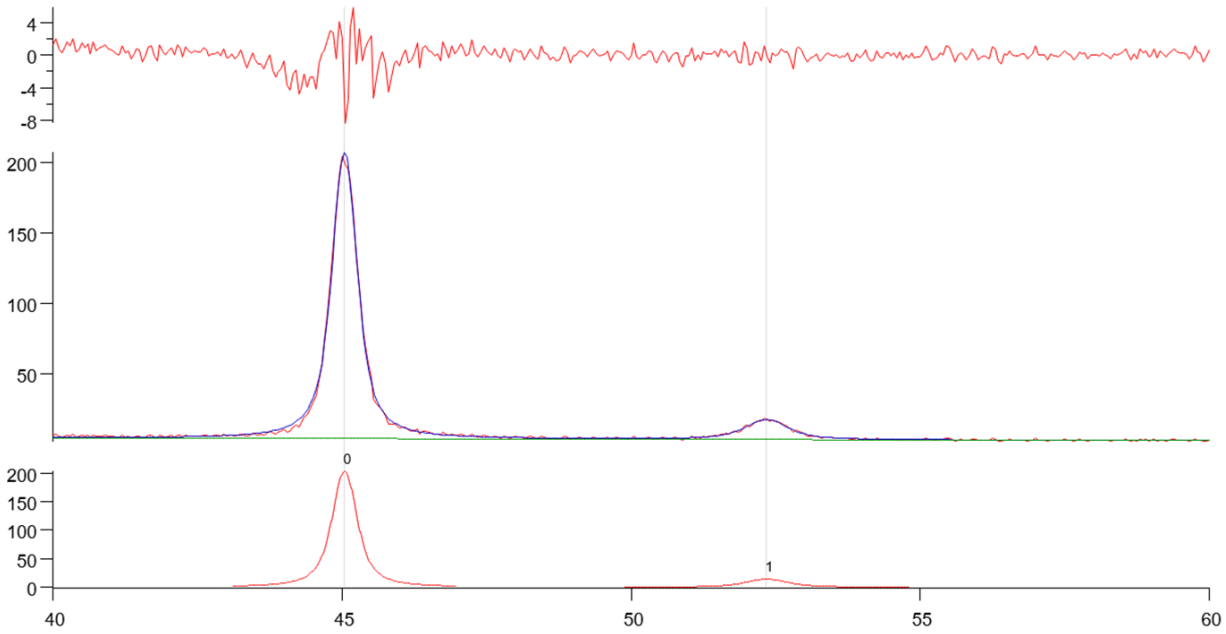

Figure 8.7: The diffraction pattern of {111} + {200} peaks at L22 ($p(H_2) = 0.1$ atm) at $\psi = 0°$.

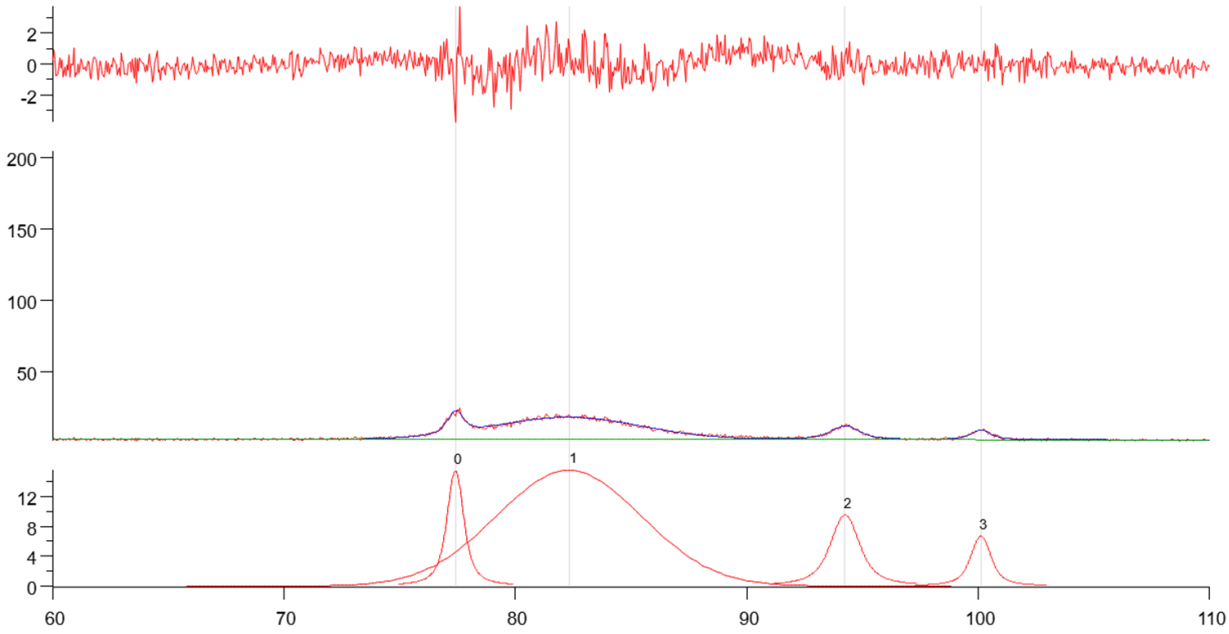

Figure 8.8: The diffraction pattern of {220} + Si/SiO_2-induced reflections + {311} + {222} peaks at L22 ($p(H_2)$ = 0.1 atm) at $\psi = 0°$.

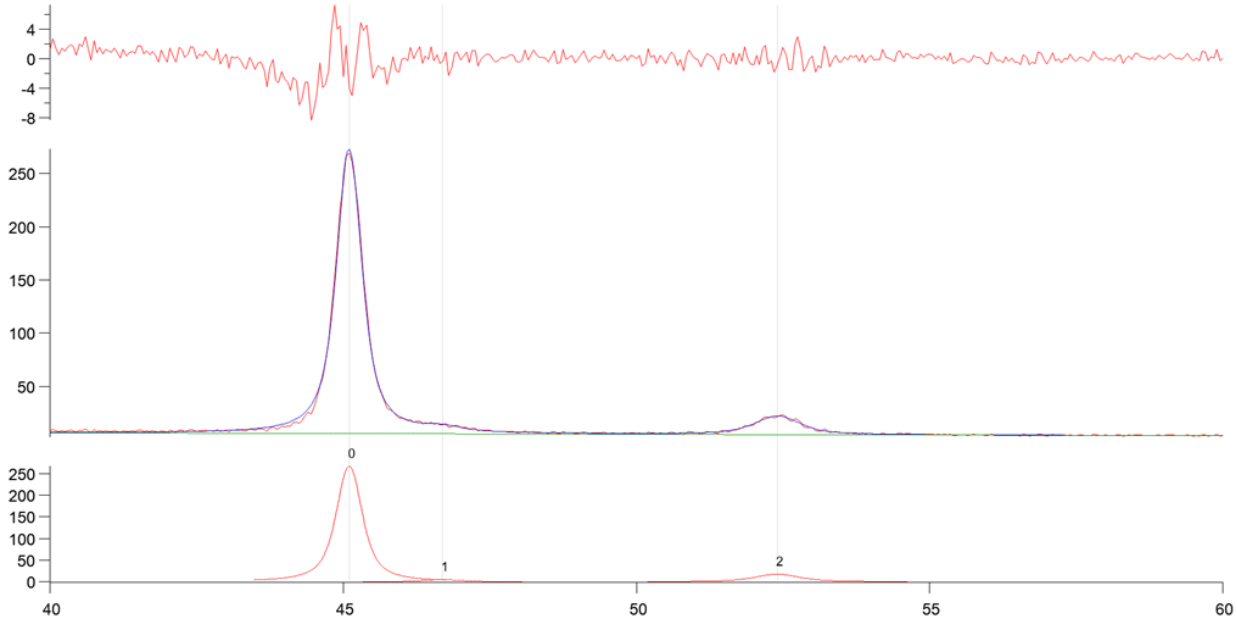

Figure 8.9: The diffraction pattern of {111} + {200} peaks at L23 ($p(H_2) = 0.05$ atm) at $\psi = 0°$.

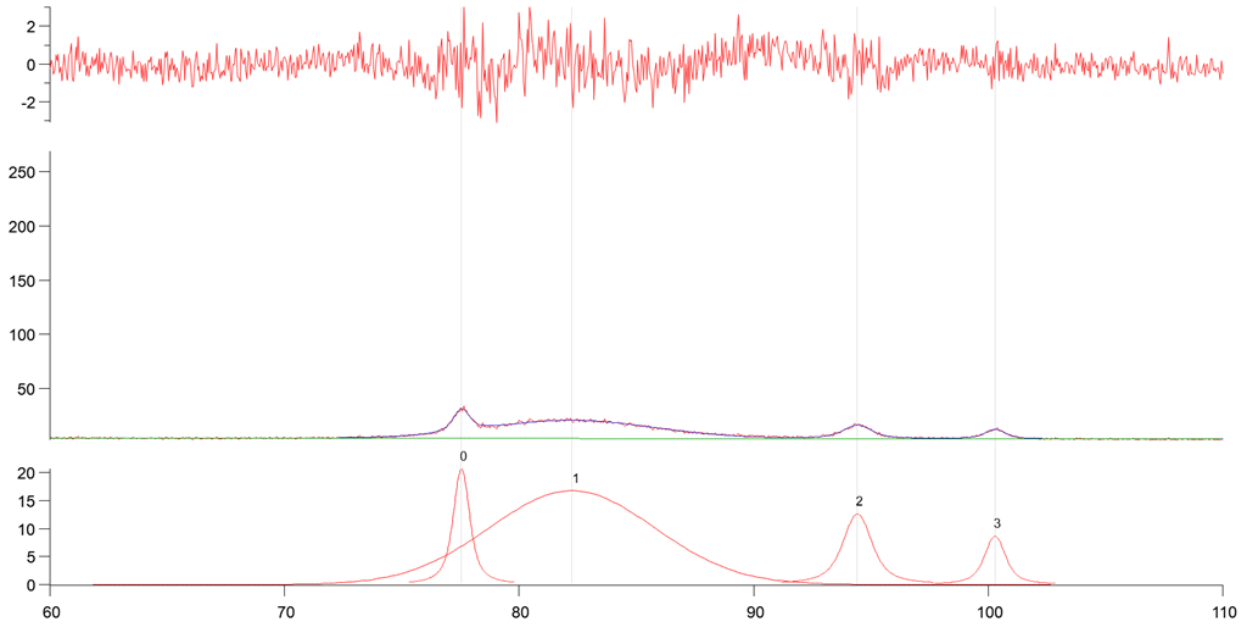

Figure 8.10: The diffraction pattern of {220} + Si/SiO_2-induced reflections + {311} + {222} peaks at L23 ($p(H_2) = 0.05$ atm) at $\psi = 0°$.

8.3. Diffraction patterns (long scans) of D21 (after loading at p(H_2) = 0.05 atm) and D22 (after loading at p(H_2) = 0.1 atm) for the open-structured Pd/Ti film

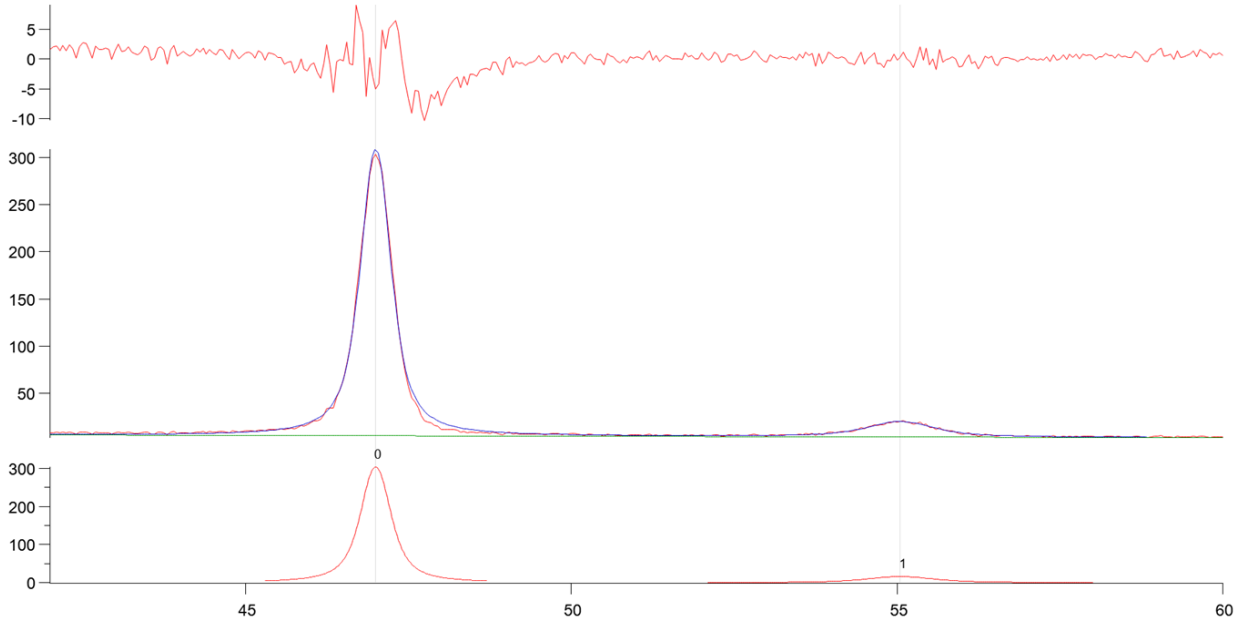

Figure 8.11: The diffraction pattern of {111} + {200} peaks at D21 (after loading at p(H_2) = 0.05 atm) at ψ = 0°.

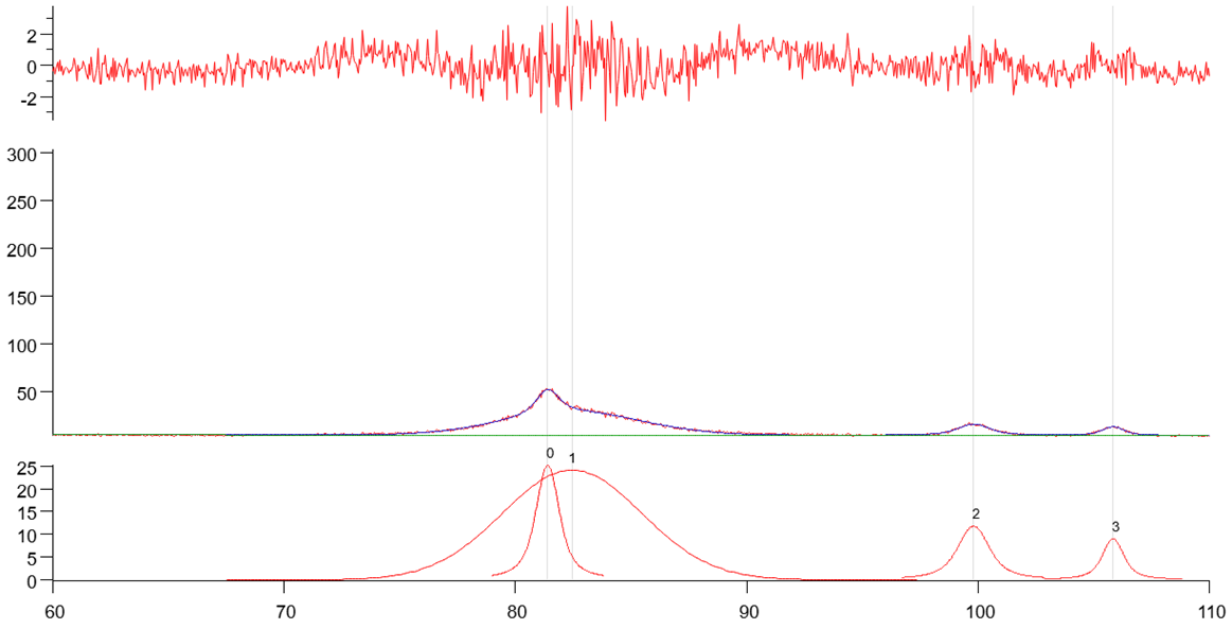

Figure 8.12: The diffraction pattern of {220} + Si/SiO_2-induced reflections + {311} + {222} peaks at D21 (after loading at p(H_2) = 0.05 atm) at ψ = 0°.

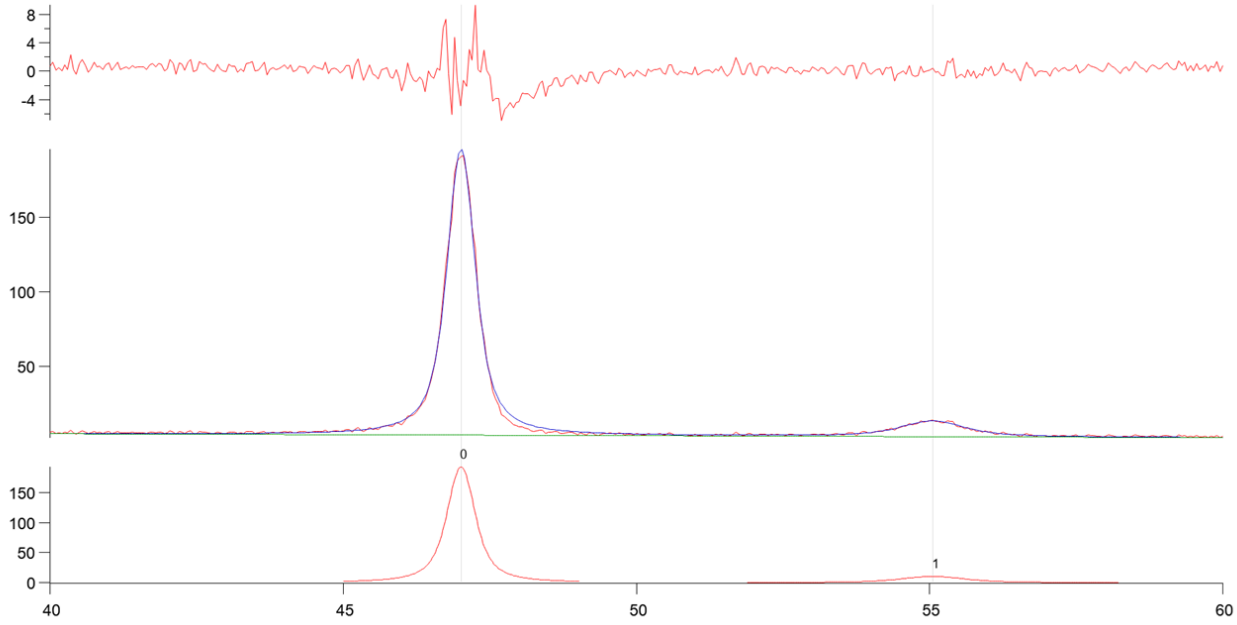

Figure 8.13: The diffraction pattern of {111} + {200} peaks at D22 (after loading at p(H_2) = 0.1 atm) at ψ = 0°.

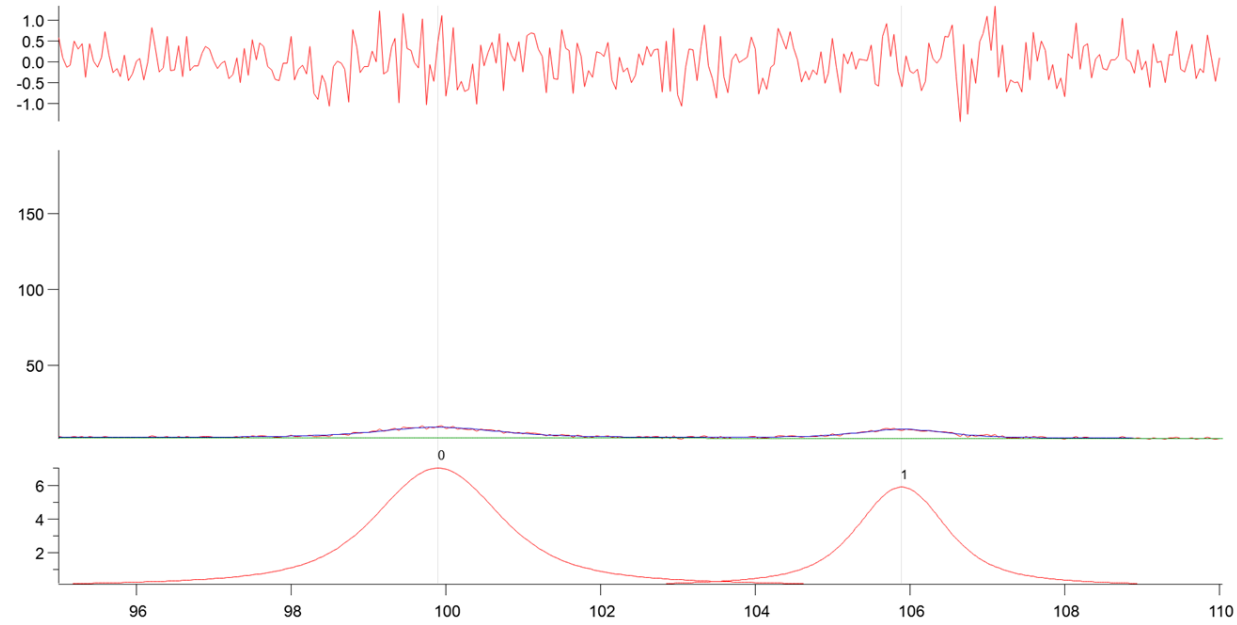

Figure 8.14: The diffraction pattern of {311} + {222} peaks at D22 (after loading at p(H_2) = 0.1 atm) at ψ = 0°.

8.4. Diffraction patterns of L2 ($p(H_2)$ = 0.05 atm), L4 ($p(H_2)$ = 0.1 atm), L5 ($p(H_2)$ = 0.05 atm), and L6 ($p(H_2)$ = 0.05 atm) for the compact-structured Pd/Ti film

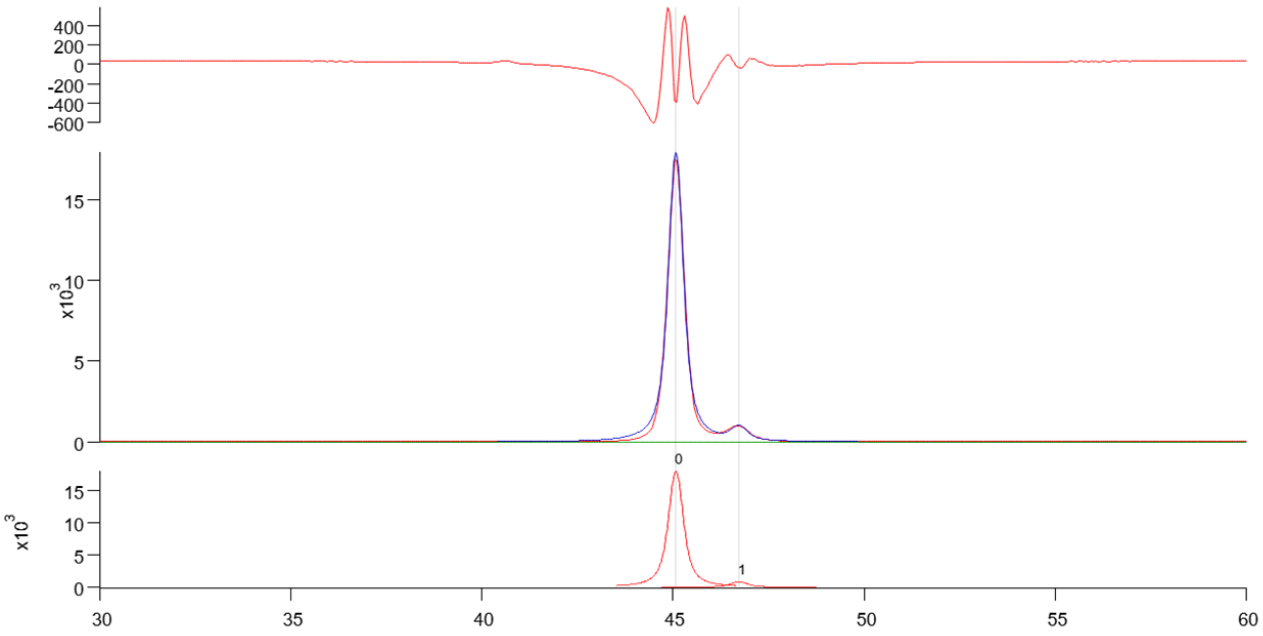

Figure 8.15: The diffraction pattern of {111} peak at L2 ($p(H_2)$ = 0.05 atm) at $\psi = 0°$.

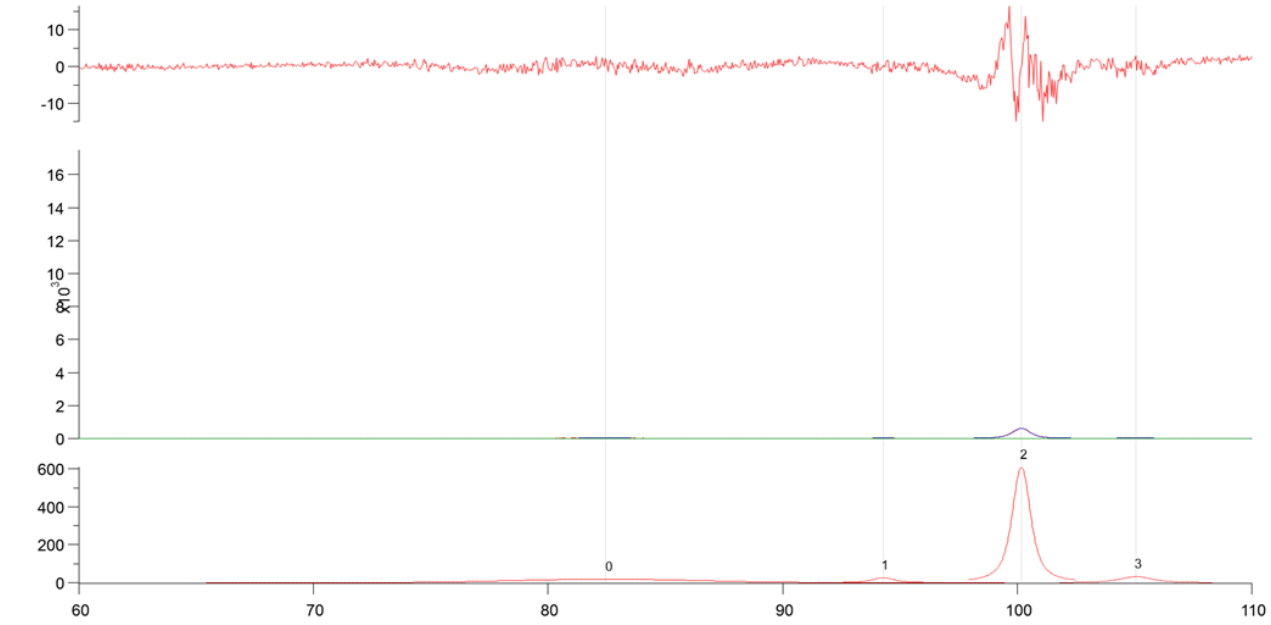

Figure 8.16: The diffraction pattern of Si/SiO_2-induced reflections + 311 + 222 peaks at L2 ($p(H_2)$ = 0.05 atm) at $\psi = 0°$.

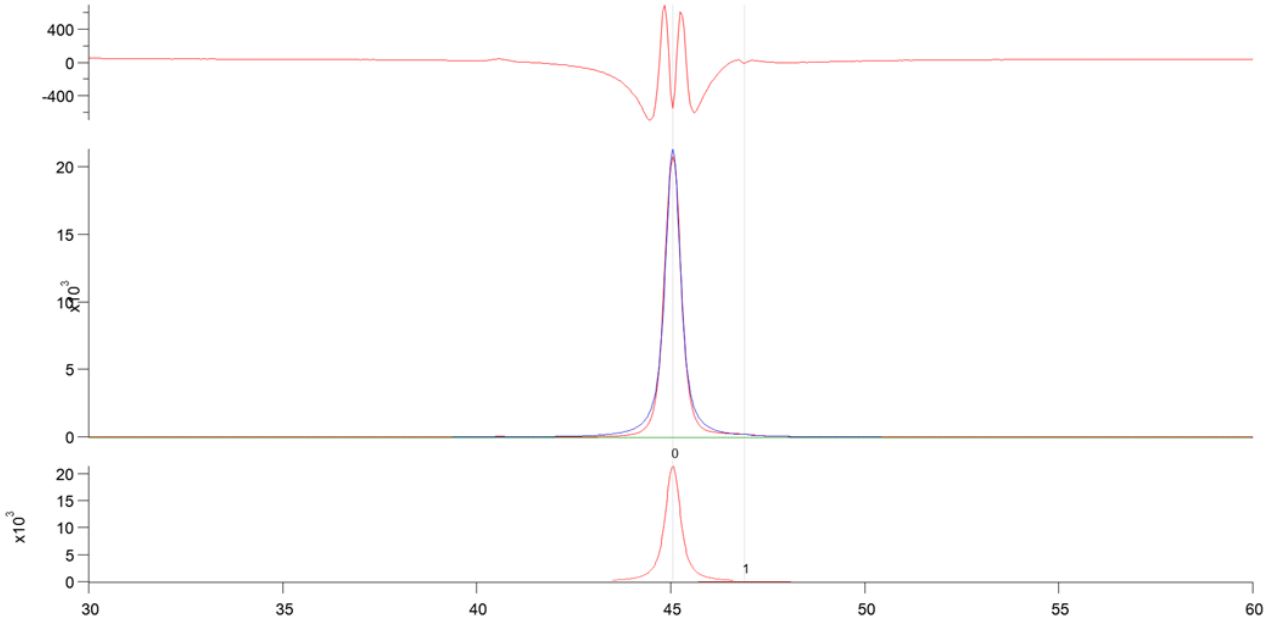

Figure 8.17: The diffraction pattern of {111} peak at L4 ($p(H_2) = 0.1$ atm) at $\psi = 0°$.

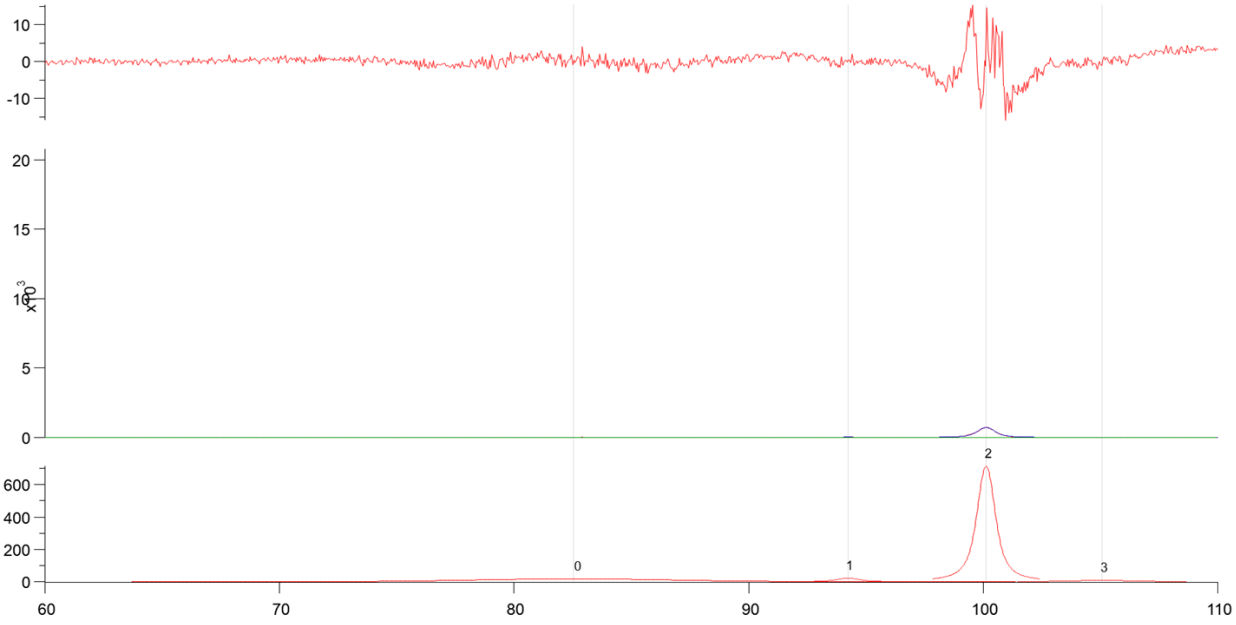

Figure 8.18: The diffraction pattern of Si/SiO_2-induced reflections + 311 + 222 peaks at L4 ($p(H_2) = 0.1$ atm) at $\psi = 0°$.

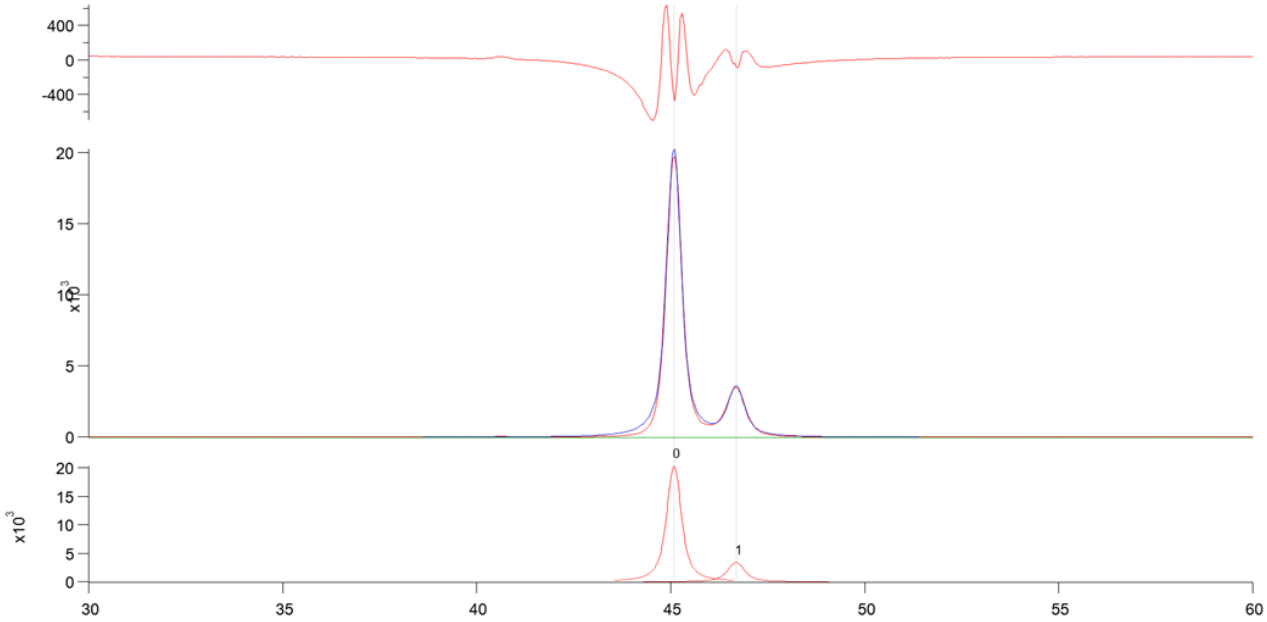

Figure 8.19: The diffraction pattern of {111} peak at L5 ($p(H_2) = 0.05$ atm) at $\psi = 0°$.

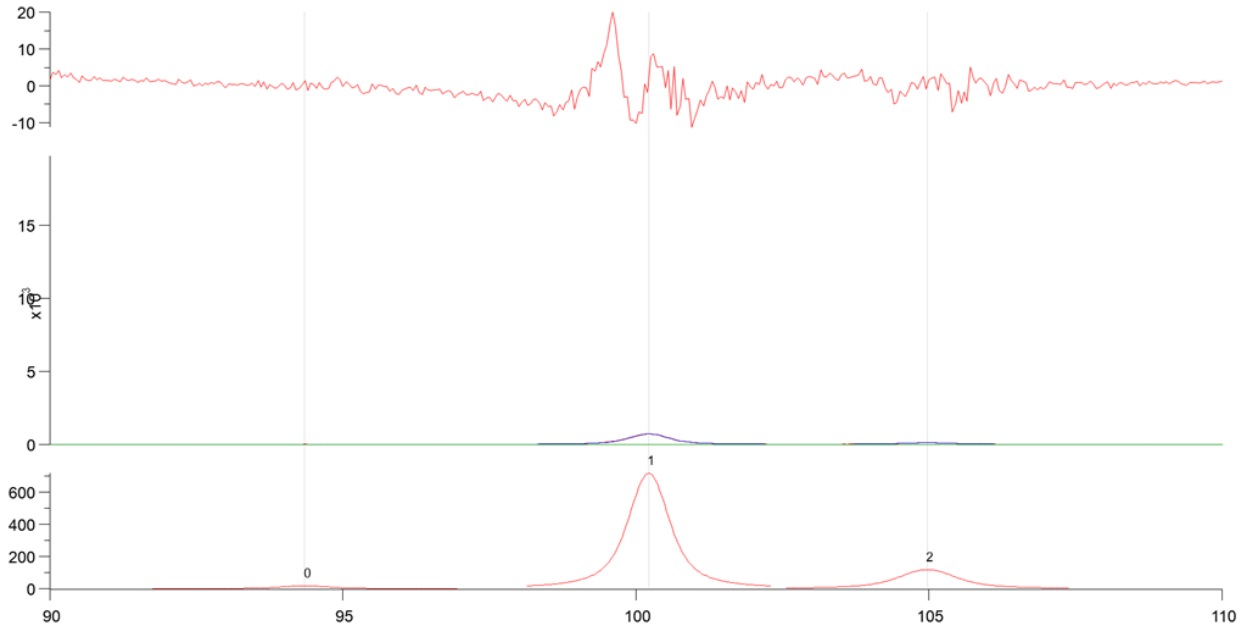

Figure 8.20: The diffraction pattern of 311 + 222 peaks at L5 ($p(H_2) = 0.05$ atm) at $\psi = 0°$.

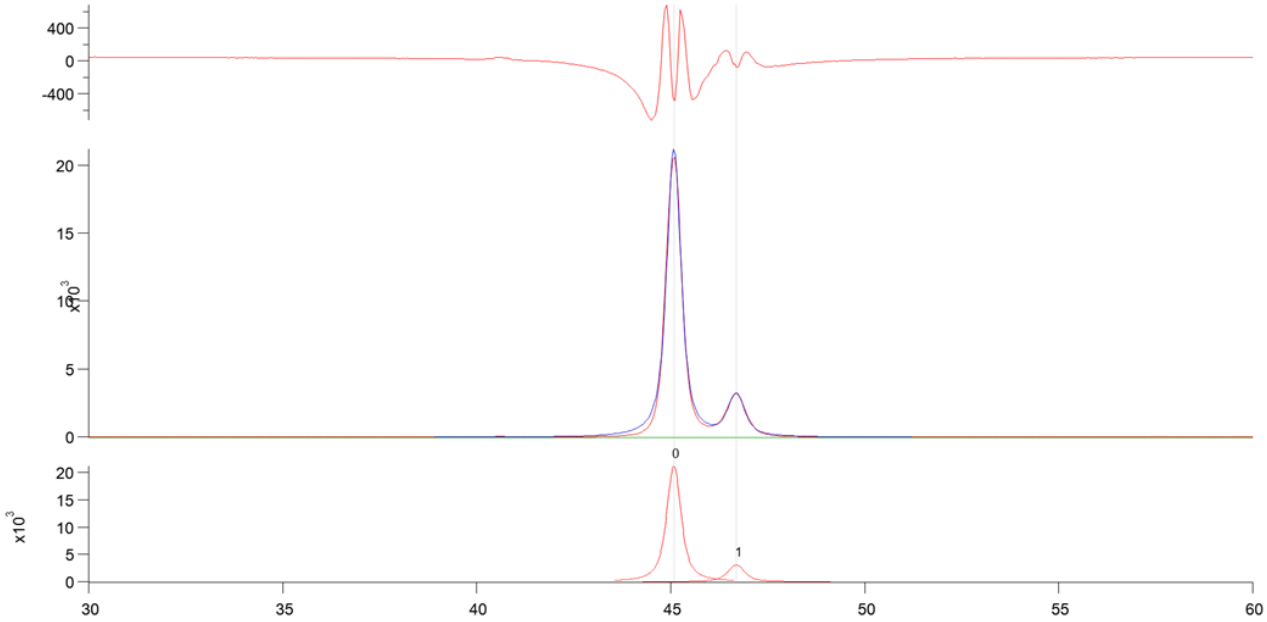

Figure 8.21: The diffraction pattern of {111} peak at L6 ($p(H_2) = 0.05$ atm) at $\psi = 0°$.

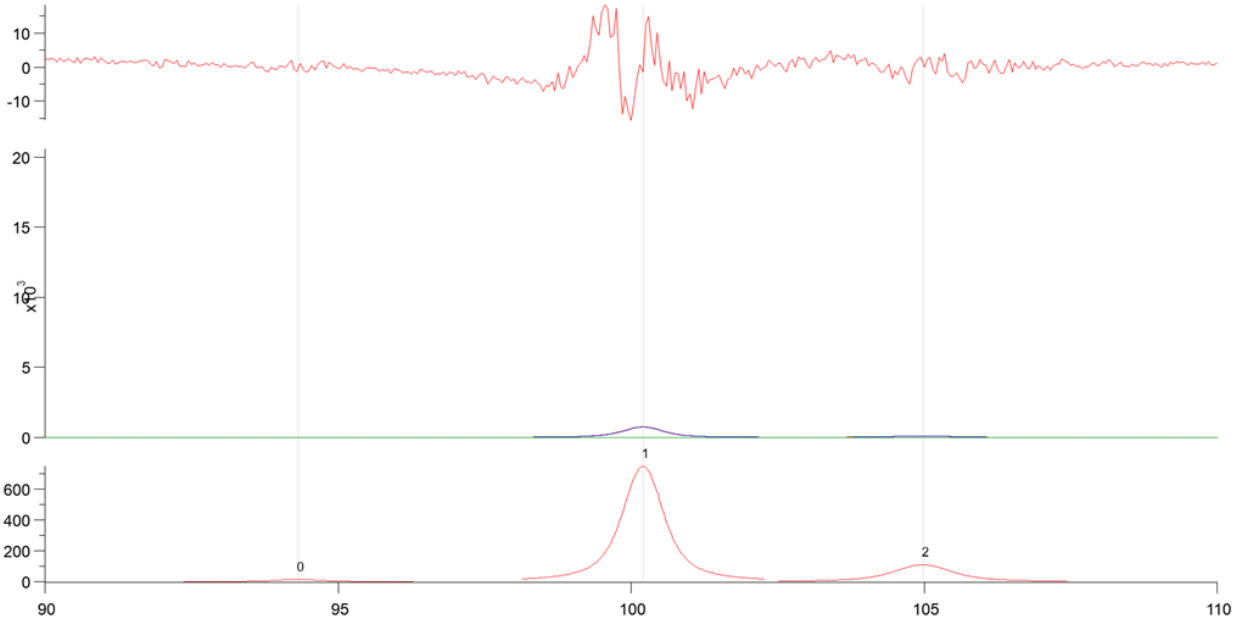

Figure 8.22: The diffraction pattern of 311 + 222 peaks at L6 ($p(H_2) = 0.05$ atm) at $\psi = 0°$.

8.5. Diffraction patterns of D4 (after loading at p(H_2) = 0.1 atm) and D5 (after loading at p(H_2) = 0.05 atm) for the compact-structured Pd/Ti film

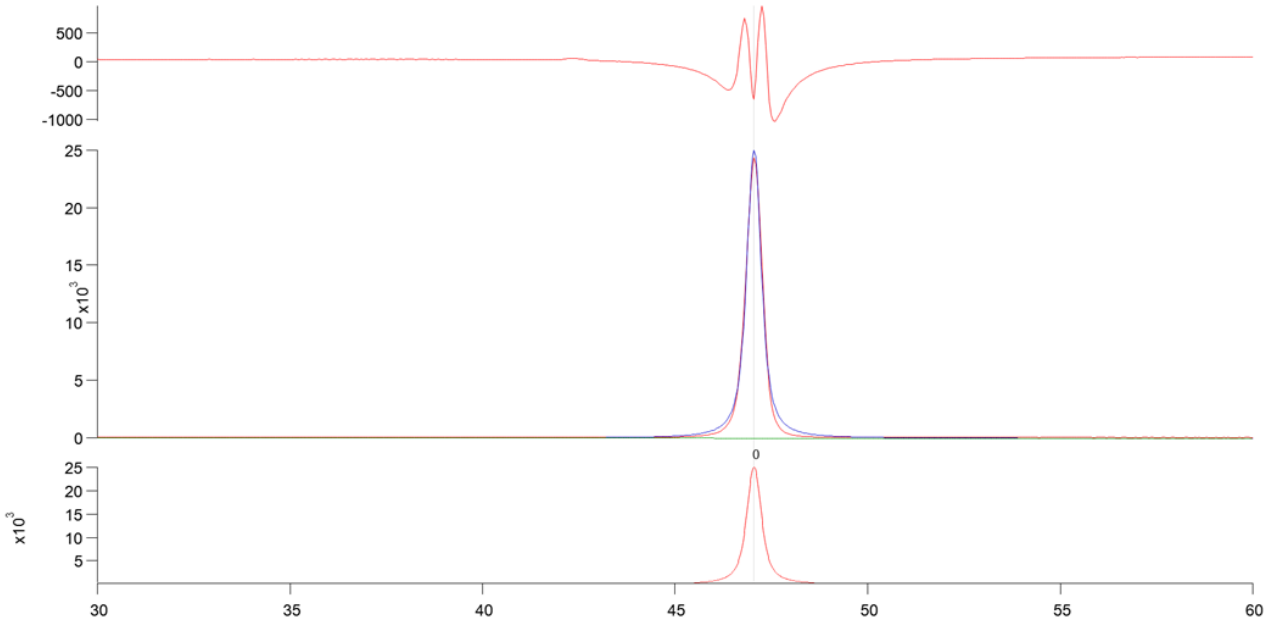

Figure 8.23: The diffraction pattern of {111} peak at D4 (after loading at p(H_2) = 0.1 atm) at $\psi = 0°$.

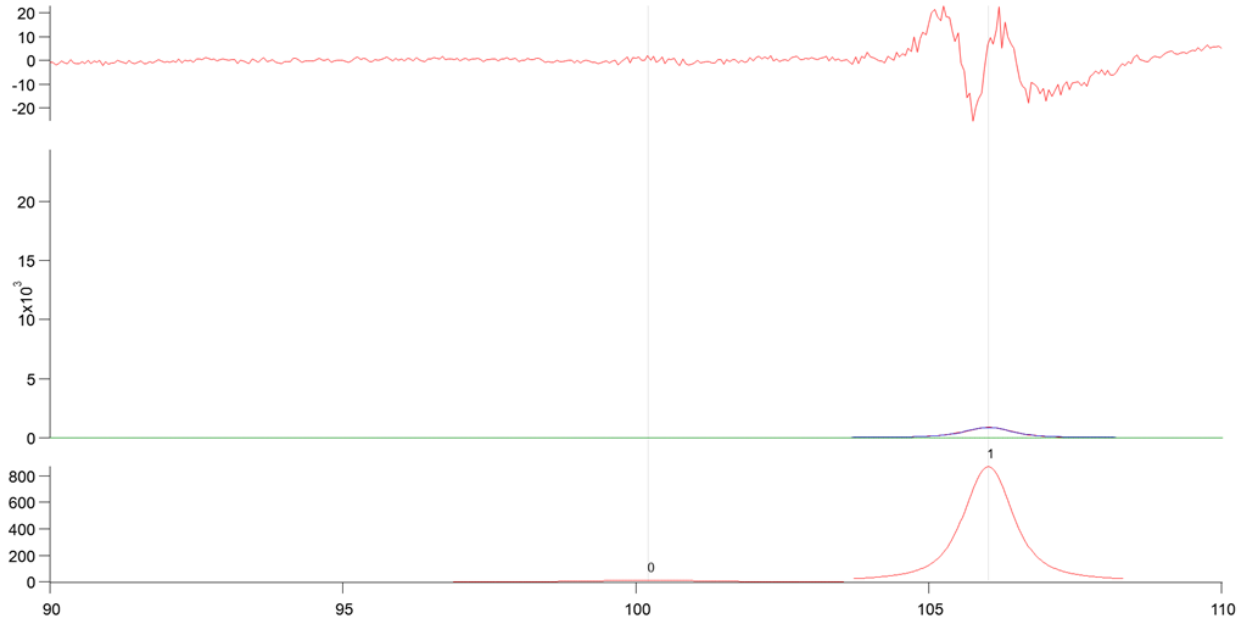

Figure 8.24: The diffraction pattern of {311} + {222} peaks at D4 (after loading at p(H_2) = 0.1 atm) at $\psi = 0°$.

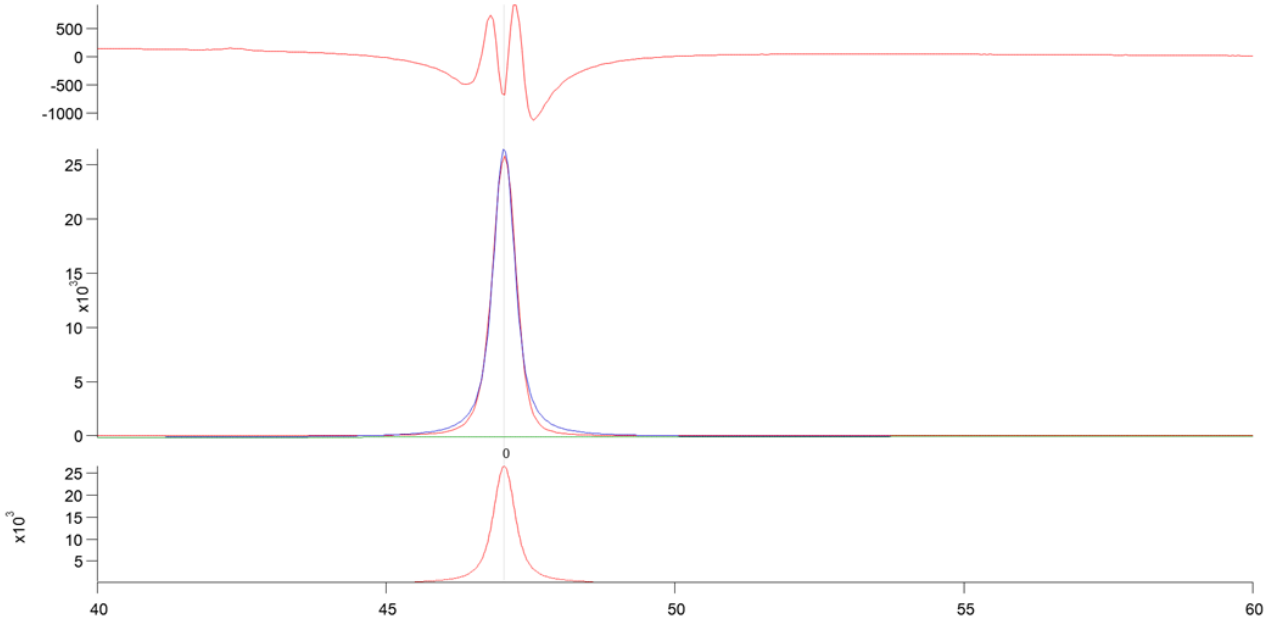

Figure 8.25: The diffraction pattern of {111} peak at D5 (after loading at p(H_2) = 0.05 atm) at $\psi = 0°$.

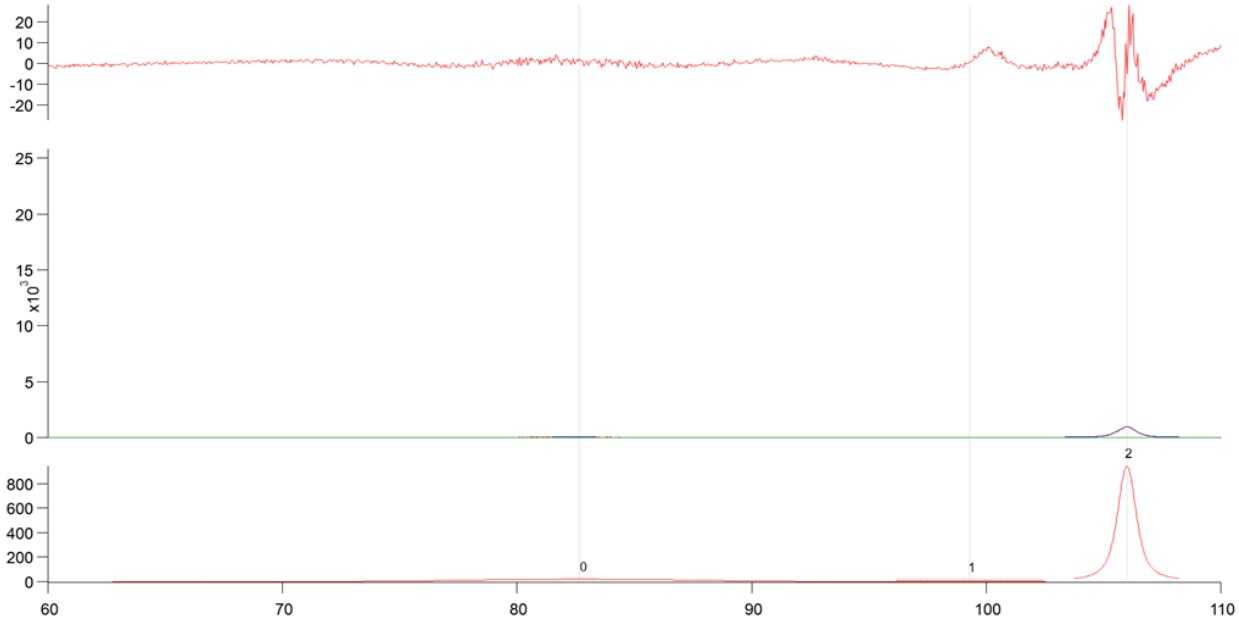

Figure 8.26: The diffraction pattern of Si/SiO_2-induced reflections + {311} + {222} peaks at D5 (after loading at p(H_2) = 0.05 atm) at $\psi = 0°$.